

XENON-129 NMR STUDIES OF GAS ADSORPTION DYNAMICS IN CRYSTALLINE
NANOTUBE MATERIALS

By

CHRISTOPHER AKEL

A THESIS PRESENTED TO THE GRADUATE SCHOOL
OF THE UNIVERSITY OF FLORIDA IN PARTIAL FULFILLMENT
OF THE REQUIREMENTS FOR THE DEGREE OF
MASTER OF SCIENCE

UNIVERSITY OF FLORIDA

2012

© 2012 Christopher Akel

To my family and friends

ACKNOWLEDGMENTS

Many people have helped me succeed throughout my graduate career at the University of Florida. First and foremost, I would like to thank my research advisor, Dr. Russ Bowers. It has been an honor and a privilege to study physical chemistry through Nuclear Magnetic Resonance under his expert guidance. His creativity, knowledge, and advice have been an inspiration throughout my time at UF, and I have gained more than merely scientific knowledge as a student in his group.

Secondly, I would like to thank Dr. Muslim Dvoyashkin, the post-doctoral student in our group with whom I collaborated with on all of these studies. Many thoughtful, creative, and insightful discussions took place between the two of us, for which I am incredibly grateful. From data analysis to planning future experiments, Dr. Dvoyashkin was instrumental in my success at the graduate school level.

I would also like to thank Ryan Wood, a senior graduate-level student in our research group. His willingness to lend his expertise in NMR and the workings of Varian software were directly responsible for some of the results contained in this thesis. Many intuitive discussions took place between him, me, and Dr. Dvoyashkin which allowed this project to come together in a scientifically responsible fashion.

Ronghui Zhou, another member of our research group with whom Dr. Dvoyashkin and I collaborated with on the design of the gas handling system also deserves recognition. The combining of the parahydrogen converter and xenon polarizer into a single but independently-functioning apparatus would not have been possible without his help.

Two more group members that I would like to thank are Hrishi Bhasse and Turgut Sonmez for their acceptance in further carrying out the research contained in this thesis

and for making good use of the xenon polarizer which was constructed during my time at UF.

On a different note, I would like to thank my committee members, Drs. Ben Smith and Thomas Mareci, for their advice and scientific expertise. Dr. Linda Shimizu of the University of South Carolina deserves gratitude for providing us with the bis-urea samples which were studied using hyperpolarized ^{129}Xe NMR. The University of Florida Department of Physics Cryogenic Services, namely Greg Labbe and John Graham, were instrumental in the successful construction of the gas handling system/xenon polarizer. Their willingness to share their proficiency in Swagelok parts and adapters and in leak-testing is greatly appreciated. In addition to this, I would like to thank the Physics and Chemistry Department's Machine Shops for all of their help and advice throughout my time here. Joe Shalosky and Todd Prox of chemistry really came through for us when our re-circulating pump died and were directly responsible for the successful construction of the oven for the xenon polarizer. Mark Link and his colleagues in physics made many small parts for us and were more than willing to offer their expertise at any time of the day, for which I am appreciative.

Finally, I would like to thank my family and friends for their support, encouragement, and understanding during my graduate career of studying NMR. Without them, none of this would have been possible.

TABLE OF CONTENTS

	<u>page</u>
ACKNOWLEDGMENTS.....	4
LIST OF TABLES.....	8
LIST OF FIGURES.....	9
LIST OF ABBREVIATIONS.....	11
ABSTRACT.....	12
CHAPTER	
1 INTRODUCTION.....	14
2 BACKGROUND.....	16
Introduction.....	16
Brief NMR Overview.....	16
¹²⁹ Xe NMR.....	18
Spin-Exchange Optical-Pumping and Hyperpolarization.....	19
Optical-Pumping.....	19
Spin-Exchange.....	22
Continuous-Flow Hyperpolarized ¹²⁹ Xe NMR.....	24
3 DESIGN AND CONSTRUCTION OF THE 129-XENON HYPERPOLARIZER.....	26
Brief Background.....	26
Polarizer Design/Construction.....	27
Sample Holder.....	29
Hyperpolarization Chamber.....	30
4 NANOPOROUS MATERIALS.....	36
L-Phenylalanyl-L-Phenylalanine.....	36
Bis-Urea Macrocycle.....	41
5 METHODS AND PULSE SEQUENCES.....	44
Spin (Hahn) Echo.....	44
Hyperpolarized ¹²⁹ Xe Tracer-Exchange.....	45
Inversion Recovery.....	48
Saturation Recovery.....	49
6 RESULTS AND DISCUSSION.....	51

L-Pheynyalanyl-L-Pheynlalanine	51
Xenon Adsorption at Various Temperatures.....	51
Tracer-Exchange	53
T ₁ Estimation	56
Bis-Urea Macrocycle.....	64
Xenon partial-pressure dependence	64
Tracer-Exchange	69
7 CONCLUSION AND RECOMMENDATIONS	71
LIST OF REFERENCES	73
BIOGRAPHICAL SKETCH.....	76

LIST OF TABLES

<u>Table</u>		<u>page</u>
2-1	NMR properties of ^1H and ^{129}Xe	18
6-1	Summary table of T_1 relaxation times.....	63

LIST OF FIGURES

<u>Figure</u>		<u>page</u>
2-1	The Nuclear Zeeman Effect.....	17
2-2	Energy-level splitting in ^{87}Rb showing optical transitions.....	20
2-3	Spin-exchange optical-pumping process inside of the pumping cell.....	23
3-1	^{129}Xe gas handling system and polarizer.....	28
3-2	Top view of the NMR probe and sample holder.....	29
3-3	Optical pumping cell for SEOP.....	31
3-4	Oven constructed for SEOP.....	32
3-5	Magnetic field of Helmholtz coils.....	33
3-6	Fiber-optic coupled laser diode array.....	34
3-7	Fully-assembled oven in the hyperpolarization chamber.....	34
3-8	^{129}Xe polarizer/gas-handling system.....	35
4-1	Schematic structure of FF.....	36
4-2	Model for the self-assembly of the FF nanotubes.....	38
4-3	Channel of FF Nanotubes.....	39
4-4	Self-assembled FF nanotubes.....	40
4-5	SEM images of FF.....	41
4-6	Bis-urea macrocycle 1.....	42
4-7	Illustration of xenon adsorption into the bis-urea macrocycle 1 nanochannels...	43
5-1	Spin (Hahn) echo pulse sequence.....	44
5-2	Illustration of the hyperpolarized NMR tracer-exchange.....	45
5-3	Tracer-exchange/selective saturation recovery pulse sequence.....	46
5-4	Single and normal file diffusion in 1D channels.....	48
5-5	Inversion recovery pulse sequence.....	49

5-6	Saturation recovery pulse sequence	50
6-1	Variable temperature hyperpolarized ^{129}Xe study on FF nanotubes.....	52
6-2	Tracer-exchange data on FF nanotubes	54
6-3	Tracer-exchange fits to the small, 1nm channels of FF	55
6-4	Tracer-exchange fits to the large, central channels of FF.....	55
6-5	Inversion recovery experiments on Xe gas reference sample at 25°C	58
6-6	Saturation recovery experiments on Xe gas reference sample at 25°C	58
6-7	Inversion recovery experiments on Xe gas reference sample at -85°C.....	59
6-8	Saturation recovery experiments on Xe gas reference sample at -85°C	59
6-9	Density and temperature dependence of ^{129}Xe spin relaxation times.....	60
6-10	Saturation recovery experiments on the small channels of FF nanotubes at - 85°C	61
6-11	Saturation recovery experiments on the small channels of FF nanotubes at - 95°C	62
6-12	Saturation recovery experiments on the large channels of FF nanotubes at - 85°C	62
6-13	Saturation recovery experiments on the large channels of FF nanotubes at - 95°C	63
6-14	Dependence of the ^{129}Xe line shape in the one-dimensional pores of bis-urea crystals on Xe partial pressure in a He/Xe mixture with a total pressure of 3115 Torr.....	65
6-15	Structure and channel diameter of ALPO-11	66
6-16	Structure of one channel in ALPO-11 indicating the three types of xenon sites.	67
6-17	^{129}Xe NMR line shapes for xenon adsorbed in ALPO-11.....	68
6-18	Tracer-exchange data on bis-urea macrocycle.....	70
6-19	Tracer-exchange fits for the bis-urea macrocycle.....	70

LIST OF ABBREVIATIONS

1D	One-dimensional
FF	L-phenylalanyl-L-phenylalanine
HP	Hyperpolarize
ND	Normal Diffusion
NMR	Nuclear Magnetic Resonance
PEEK	Polyether Ether Ketone
PFA	Perfluoroalkoxy
Rb	Rubidium
RF	Radiofrequency
SEM	Scanning Electron Microscopy
SEOP	Spin-Exchange Optical-Pumping
SFD	Single-File Diffusion
XE	Xenon

Abstract of Thesis Presented to the Graduate School
of the University of Florida in Partial Fulfillment of the
Requirements for the Degree of Master of Science

XENON-129 NMR STUDIES OF GAS ADSORPTION DYNAMICS IN CRYSTALLINE
NANOTUBE MATERIALS

By

Christopher Akel

August 2012

Chair: Clifford R. Bowers
Co-Chair: Benjamin W. Smith
Major: Chemistry

Nanotube materials have a wide range of practical applications in the field of chemistry. Characterizing one-dimensional (1D) nanotubular systems is vital in regards to optimizing their applications. In channels large enough for molecules to pass by one another, normal diffusion (ND) is observed where the mean-squared displacement is proportional to the observation time. In contrast, nanotubes having channels too small for molecules to pass one another exhibit single-file diffusion (SFD). In this case, one may expect a square-root time dependency of the mean-squared displacement.

To achieve the results of this study, a ^{129}Xe polarizer and gas handling system was built to allow for spin-exchange optical pumping (SEOP) of rubidium metal which is the process utilized to hyperpolarize xenon gas in our lab. This involved the design and construction of an oven for the optical pumping cell, the re-designing of the entire gas handling system previously built in our lab, and the design of a new and larger optical pumping cell.

Continuous-flow hyperpolarized ^{129}Xe nuclear magnetic resonance (NMR) was then employed to systematically investigate adsorption dynamics of xenon (Xe)

occurring in two different 1D nanotubular materials: self-assembled L-phenylalanyl-L-phenylalanine (FF) and self-assembled bis-urea macrocycles. The channel diameters of FF and the bis-urea macrocycle are $\sim 10\text{\AA}$ and $\sim 4\text{\AA}$, respectively. FF also possesses a large central channel with a diameter of approximately 100nm. Upon cooling of the sample to temperatures below -75°C , xenon adsorption into the smaller channels of FF is observed, whereas adsorption into the larger channel is present at all temperatures studied.

It was demonstrated through saturation and inversion recovery experiments that a temperature dependence exists for T_1 in FF nanotubes. As the temperature is decreased, T_1 gets shorter. Alternatively, as the temperature was decreased, the chemical shift of the adsorbed phases increased. Temperature discrepancies between the tracer-exchange and saturation recovery experiments made it difficult to directly compare the T_1 values. This was due to a warming effect of the sample in the continuous-flow experiments caused by the flow-rate and gas stream.

The Xe partial-pressure dependence study performed on the bis-urea macrocycle demonstrated that the chemical shift anisotropy was axially symmetric and positive at low loading and then lost its axial symmetry with increased loading. The tracer-exchange experiments were inconclusive in regards to the type of diffusion occurring in the channel. This study, along with the FF experiments, demonstrates that Xe NMR can be utilized to obtain large amounts of information in regards to adsorption dynamics and characteristics of crystalline nanotubular materials.

CHAPTER 1 INTRODUCTION

In recent years, nanoporous materials with one-dimensional (1D) channels have been studied intensively due to their possible applications to gas storage, separation, and catalysis.¹ Diffusion of gases through these 1D channels represents the primary focus of this thesis. Nanoporous materials possessing 1D channels with diameters that are sufficient to allow for particles inside of the channel to pass one another will exhibit normal diffusion, where the mean-squared displacement is proportional to the observation time. For channels too narrow to allow for the mutual passing of particles, single-file diffusion may be observed in which the mean-squared displacement is proportional to the square-root of the observation time.

Xenon-129 Nuclear Magnetic Resonance is a spectroscopic technique that is well-suited to the study of nanoporous solids.² Benefits of ^{129}Xe NMR include its large chemical shift range which is sensitive to the size, shape, and loading of nanopores and its long T_1 relaxation time which leads to a larger range of achievable observation times. Given these characteristics, a physisorbed phase can readily be distinguished from a bulk gas phase inside of a 1D nanochannel by a chemical shift which helps reveal the interactions of xenon atoms with the surfaces of the solid. Accordingly, ^{129}Xe NMR has been utilized to study the structures of solids such as zeolites³, polymers⁴, nanotubes⁵, and proteins⁶.

Given the fact that conventional NMR suffers from inherently small signals, hyperpolarized ^{129}Xe NMR has been developed to improve sensitivity.⁷ Hyperpolarized ^{129}Xe NMR signals can be up to four orders more intense in comparison to signals obtained from thermally-polarized ^{129}Xe NMR.⁸ Contained in this thesis is the

application of continuous-flow hyperpolarized ^{129}Xe NMR spectroscopy to nanoporous solids containing 1D channels to explore xenon gas adsorption and diffusion within the nanochannels.

Chapter 2 of this thesis will give a brief background of the essential topics necessary for understanding this thesis. Chapter 3 will give a detailed account of the ^{129}Xe polarizer and gas-handling system that was constructed so that these experiments could be carried out. Chapter 4 will describe the nanoporous materials that were studied while Chapter 5 introduces the reader to the methods and pulse sequences that were to acquire the data, which is presented in Chapter 6. Finally, Chapter 7 will sum up the results through a conclusion as well as offer suggestions and recommendations for future studies.

CHAPTER 2 BACKGROUND

Introduction

Chapter 2 represents a brief overview of NMR and hyperpolarized NMR that will be critical to understanding the remaining chapters of this thesis. Section 2.2 will focus on the basics of NMR whereas section 2.3 will identify the physical properties and applications of ^{129}Xe . Section 2.4 will discuss the technique of spin-exchange optical pumping which is the method commonly utilized to hyperpolarize noble gases such as xenon to enhance the sensitivity of NMR, and finally, section 2.5 will discuss the technique of continuous-flow hyperpolarized ^{129}Xe NMR.

Brief NMR Overview

Nuclear magnetic resonance is the phenomenon where electromagnetic radiation is absorbed and re-emitted by nuclei in a magnetic field. This energy is at a specific resonance frequency which is dependent on the magnetic properties of the nuclei of interest and the strength of the magnetic field. Isotopes having an odd number of protons and/or neutrons (nonzero spin) have a magnetic moment and possess angular momentum and can be studied using NMR.⁹ When a static external magnetic field (B_0) is applied, it interacts with the magnetic dipole moment of the nuclei causing the spins to order preferentially along the magnetic field. This creates a difference in the energy levels and is referred to as the Nuclear Zeeman Effect, which is represented in Figure 2-1 and forms the basis for all NMR experiments.

The NMR signal is proportional to the difference in the populations of the spin states. Each spin state is populated according to a Boltzmann distribution:

$$\frac{N_\alpha}{N_\beta} = e^{-\Delta E/kT} \quad (2-1)$$

where N_α and N_β represent the number of spins in the α and β states, respectively, ΔE is the energy difference arising from the Nuclear Zeeman Effect, k is the Boltzmann constant, and T is the temperature.⁹

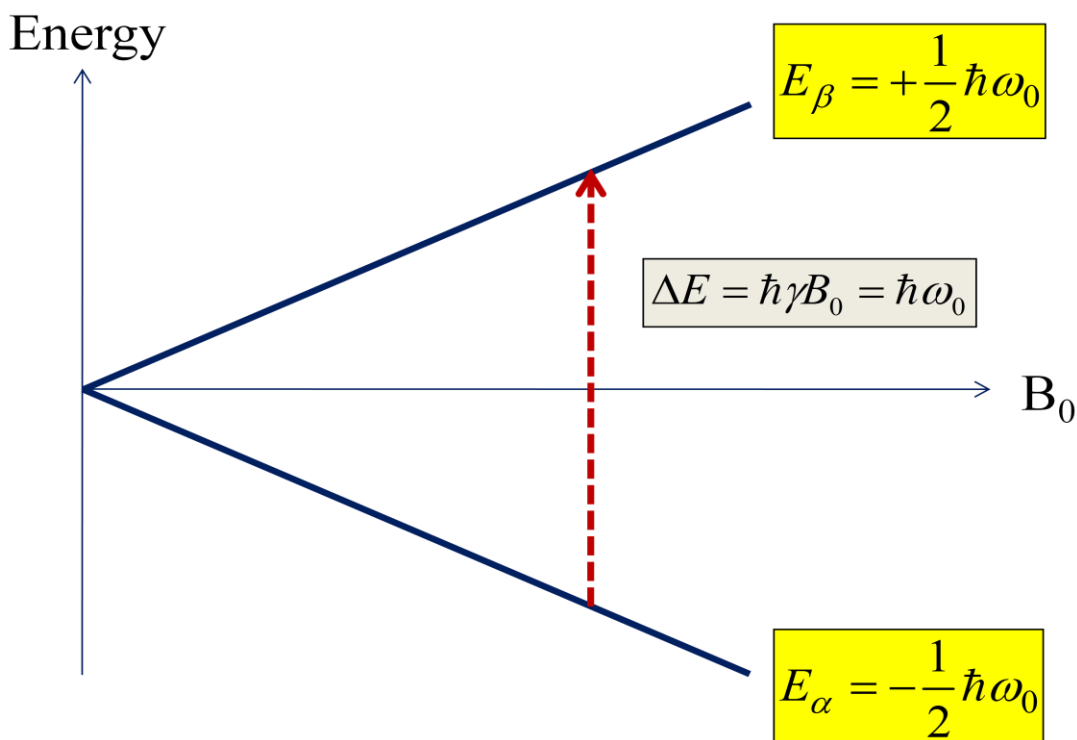


Figure 2-1. The Nuclear Zeeman Effect

As mentioned previously, NMR suffers from inherently low sensitivity. This can be demonstrated using standard values for a proton in the presence of a 400 MHz (9.4T) external magnetic field, whereas the ΔE would be approximately 2.66×10^{-25} J. Using this ΔE value and Equation (2-1) at standard temperature, one obtains $\frac{N_\alpha}{N_\beta} = 1.000064$. This represents a very small difference in the spin state populations of the α and β states which correlates to a small signal thus rendering NMR quite insensitive. However, a technique known as hyperpolarization, which seeks to increase the

difference in the populations of the spin states, can be utilized to overcome this insensitivity.

¹²⁹Xe NMR

Xenon has a molecular weight of 131.29 grams per mole. It contains 54 electrons and has the electron configuration [Kr] 4d¹⁰5s²5d⁶. Of the many stable isotopes of xenon, two have a nonzero spin and can be studied using NMR: ¹²⁹Xe with $I = 1/2$ and ¹³¹Xe with $I = 3/2$. It was first applied to NMR in 1982 by Fraissard and Ito.¹⁰

Xenon is a noble gas meaning that its external electronic orbital is completely occupied. As such, it is chemically inert. At standard temperature and pressure, xenon exists as a gas. Given its standard boiling and melting points of 165.02K and 161.38K, respectively, both solid and liquid phases can readily be obtained within most laboratory environments.¹¹ The long T₁ relaxation time of ¹²⁹Xe makes it a favorable candidate for hyperpolarized NMR experiments.

Table 2-1. NMR properties of ¹H and ¹²⁹Xe

Nuclei	¹ H	¹²⁹ Xe
Spin, I	$1/2$	$1/2$
Magnetogyric Ratio (10 ⁸ s ⁻¹ Tesla ⁻¹)	2.675	-0.74
Natural Abundance, (%)	99.99	26.44

As can be seen above in Table 2-1, ¹²⁹Xe has a much lower magnetogyric ratio and natural abundance than ¹H. Together, these combine to make the NMR sensitivity for ¹²⁹Xe much worse than for ¹H at thermal equilibrium. As a result, signal averaging must be employed to increase the signal-to-noise ratio in NMR experiments when

working with thermally-polarized ^{129}Xe . As mentioned previously, however, this can be overcome through hyperpolarization of xenon which will be discussed shortly.

Xenon-129 is a monatomic gas possessing a spherically-symmetric electron cloud. Any distortion to this cloud is reflected in the chemical shielding of the nucleus which in turn will be observed as a change in the NMR chemical shift. Hence, ^{129}Xe has a chemical shift that is very sensitive to interactions with the local environment which again makes it an ideal candidate for the study of nanoporous materials.¹¹

Spin-Exchange Optical-Pumping and Hyperpolarization

Spin-exchange optical-pumping (SEOP) is the primary method used to hyperpolarize gases such as ^{129}Xe , ^{83}Kr and ^3He .¹² This method is suitable for producing large amounts of hyperpolarized gases for NMR measurements as well as medical imaging.

Optical-Pumping

Optical-pumping begins with an alkali-metal vapor. In this first step of the SEOP process, angular momentum is transferred from circularly-polarized photons of light to alkali metal electrons. This process was developed by Kastler in 1957, for which he was awarded the Nobel Prize for Physics.¹³

Rubidium is often the alkali-metal of choice for the creation of hyperpolarized gas through SEOP due to its large spin-exchange cross sections, relatively high vapor pressures at moderate temperatures, and the availability of high-power light sources that emit electromagnetic radiation at its *D*-line absorption wavelengths, which can be seen in Figure 2-2.¹⁴ Two stable isotopes of rubidium exist in nature: ^{85}Rb with $I = 5/2$ and a natural abundance of 72.2%, and ^{87}Rb with $I = 3/2$ and a natural abundance of 27.2%. The total electronic angular momentum is represented by $\vec{J} = \vec{S} + \vec{L}$, where \vec{S} is

the electron spin and \vec{L} is the orbital angular momentum.¹¹ The total atomic angular momentum is represented by $\vec{F} = \vec{J} + \vec{I}$. In the presence of an external magnetic field, B_0 , the Hamiltonian is:^{11,12,15}

$$\hat{H}_{Rb} = A\mathbf{I} \cdot \mathbf{S} + \left(g_s \mu_B S_z - \frac{\mu_I}{I} I_z \right) B_0 \quad (2-2)$$

where A is the hyperfine coupling constant and \mathbf{I} and \mathbf{S} are the nuclear and electron spins of rubidium, respectively. The next two terms are representative of the magnetic-dipole couplings of the electron and nuclear spins to the magnetic field, B_0 , where g_s is the g-factor of an electron, or -2.00232. I corresponds to the nuclear spin quantum number. The Bohr magneton and nuclear magnetic moment are represented by μ_B and μ_I , respectively. To ensure that the hyperfine interaction is dominant, which is the first term in Equation (2-2), a weak magnetic field of approximately 10-20 gauss is commonly used to optically-pump rubidium for spin exchange applications.

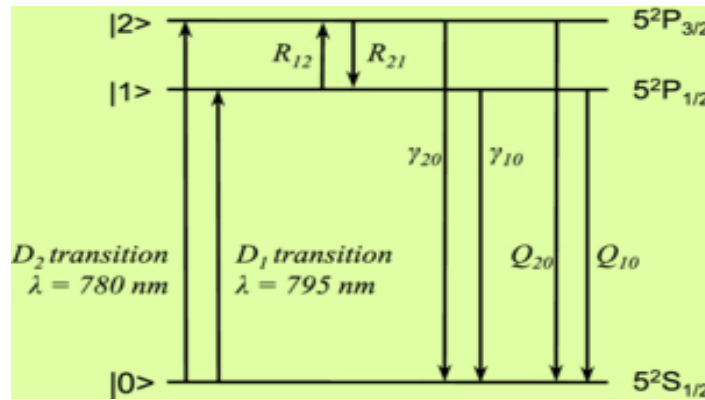


Figure 2-2. Energy-level splitting in ^{87}Rb showing optical transitions

Figure 2-2 shows the energy levels and transition wavelengths of ^{87}Rb . Electrons in the ground state can be excited to higher energy states by absorbing photons at the D-transitions. The D_1 transition is most commonly used for optical pumping of rubidium and this wavelength of light was used throughout all of our SEOP experiments.

The rubidium atom is spherically symmetric with an orbital spin of $L=0$. It possesses one optically-active electron having an orbital angular momentum of 0, 1, 2, etc. and an electron spin of 1/2. The spin-orbit coupling results in a total momentum of $\vec{J} = 1/2$. As a result of this coupling, the first excited energy level with an orbital angular momentum of $L = 1$ splits into a $^2P_{1/2}$ and a $^2P_{3/2}$ state. With optical absorption from the ground state of $^2S_{1/2}$ to the $^2P_{1/2}$ and $^2P_{3/2}$, the doublet D_1 and D_2 transitions are observed.¹²

In optical pumping, a heated glass cell containing rubidium vapor is placed in a relatively weak magnetic field and is irradiated with σ_+ circularly-polarized light at the D_1 transition wavelength of approximately 795 nm. The absorption of light excites transitions between the various Zeeman levels according to the selection rules. The excited states decay spontaneously back to the ground state and re-emit π , σ_+ , and σ_- light in all spatial directions.¹⁵

The irradiation of the atomic vapor within the pumping cell using circularly-polarized light induces a polarization of the rubidium. This occurs through the process of depopulation optical pumping, where the circularly-polarized light passes angular momentum to the rubidium vapor atoms.

Through a combination of irradiation with σ_+ circularly-polarized light and relaxation back to the ground state, a strong non-thermal equilibrium polarization of the ground state can be induced.¹⁵ Once polarization of the rubidium has been achieved through irradiation and optical-pumping, transfer of spin angular momentum from the alkali-atom to the Xe nuclear spin can occur by the process of spin-exchange within the pumping cell.

Spin-Exchange

Inside of the pumping cell and during spin-exchange collisions, the rubidium electron gets flipped due to its coupling with the nuclear spin of colliding xenon atoms, which can be seen in Figure 2-3. The hyperfine interaction between the electron spins and the nuclear spins of the noble gas is:

$$A\mathbf{S} \cdot \mathbf{I} = \frac{A}{2}(S^+I^- + S^-I^+) + AS_zI_z \quad (2-3)$$

Where again, A is the hyperfine coupling constant that is dependent on the distance between the electron and the nucleus, and \mathbf{I} and \mathbf{S} are the nuclear and electron spins of rubidium, respectively. The term in parenthesis of Equation (2-3) allows spin exchange to happen.¹⁵

Buffer gases such as nitrogen and helium are often mixed with the rubidium vapor inside of the pumping cell to increase efficiency of the optical-pumping process. Nitrogen prevents radiation trapping because it nonradiatively de-excites, or quenches, the excited rubidium atoms before they have a chance to re-radiate a photon.¹² Helium allows for pressure broadening of the D_1 absorption line. This results from collision interactions between the rubidium electron cloud and the buffer gases and helps to improve absorption efficiency of the light sources emitting radiation at the D_1 transition of about 795 nm.¹¹ When atoms of rubidium collide with buffer gases, a mixing of atomic sublevels occurs. It has been reported by Walker and Happer that the efficiency of the optical pumping process can be enhanced by a factor of 1/3 to 1/2 due to the collision-mixing of the rubidium excited states.¹⁵

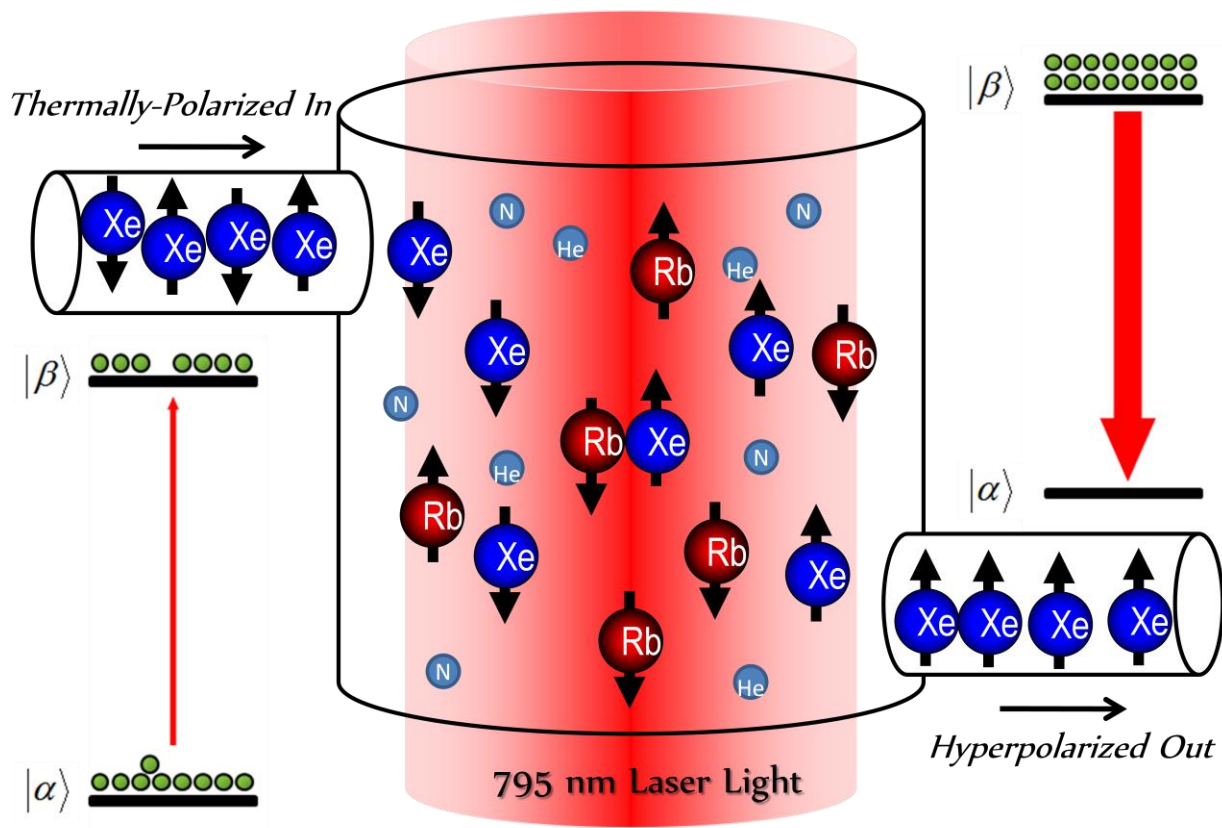


Figure 2-3. Spin-exchange optical-pumping process inside of the pumping cell

As seen in Figure 2-3, thermally-polarized xenon, with only a slight population difference between the α and β states which translates to a small NMR signal, enters the pumping cell. Inside of the pumping cell, which is also in the presence of an external magnetic field (not shown), rubidium vapor is optically pumped by 795 nm laser light. Xenon atoms collide with polarized rubidium atoms and through spin exchange, xenon becomes hyperpolarized and exits the pumping cell. As can be seen on the right side of Figure 2-3, after the process of SEOP, there exists a large difference between the populations of the α and β states which correlates to a vastly improved NMR signal. This deviation from the thermal equilibrium populations of the alpha and beta states is what is referred to as hyperpolarization throughout this thesis.

Continuous-Flow Hyperpolarized ^{129}Xe NMR

Thermally-polarized ^{129}Xe NMR suffers from long acquisition times resulting from its long T_1 relaxation time and low spin polarization. Together, these create the need for a fairly long recycle delay and much signal averaging resulting in lengthy experiments. Using hyperpolarized ^{129}Xe through the SEOP process just discussed, NMR sensitivity can be drastically increased.

Prior to the use of continuous-flow, hyperpolarized xenon experiments were carried out using a batch method developed by Pines and others.¹⁶ During this process, a pumping cell having valves is filled with rubidium metal and a mixture of xenon and buffer gases. After the rubidium has been optically pumped and the polarization transferred to xenon, the gas mixture containing hyperpolarized xenon is expanded into the NMR probe. This process works well but the development of a continuous-flow apparatus has made the entire process much more efficient.

The method of continuously-flowing the hyperpolarized ^{129}Xe throughout NMR measurements was developed by Happer and others and represents the technique utilized throughout the studies contained in this thesis.¹²

During the process of continuous-flow hyperpolarized ^{129}Xe NMR, a gas re-circulating pump constantly refreshes the xenon inside of the pumping cell and the NMR probe at a flow rate of approximately 75-150 ml/min. This range gives ample time for the ^{129}Xe gas to interact with the rubidium atoms inside of the pumping cell and become hyperpolarized. Upon exiting the pumping cell, the xenon gas mixture flows through the sample that is contained in the NMR probe and the signal is acquired. In contrast to the batch method previously discussed, continuous-flow experiments do not rely on any sort of gas expansion to transfer the hyperpolarized xenon to the NMR probe. Instead, it

takes advantage of retaining the high xenon spin polarizations throughout the entire NMR experiment. Utilizing this method allows for the spin polarizations to be replenished on a time-scale that is dependent on the flow rate and not the T_1 relaxation time. Accordingly, the recycle delay for the experiments is no longer limited by the long longitudinal relaxation time of xenon. This allows for phase cycling, signal averaging, and 2D NMR experiments on a plausible time-scale.

Over the years, many continuous-flow hyperpolarized ^{129}Xe NMR apparatuses have been designed with their main goal being to maximum xenon polarization that can be transferred to NMR samples.^{17,18} Many experimental variables such as laser power, gas pressure and composition, and flow rate have been analyzed to optimize xenon polarization.¹⁹ Accordingly, using all of the available information and taking into account previous design flaws and successes, an apparatus was developed in our lab to efficiently polarize xenon in a continuously-flowing operational mode and capably transfer this hyperpolarized xenon to our NMR probe and sample. Chapter 3 will discuss, in detail, the xenon polarizer that was designed, built, and utilized in our lab for NMR studies of nanoporous solids and other materials.

CHAPTER 3 DESIGN AND CONSTRUCTION OF THE ^{129}Xe HYPERPOLARIZER

Brief Background

In our lab, a ^{129}Xe polarizer was previously built by Zook, a former graduate student.¹⁷ In 2005, this polarizer was re-designed by Cheng, another former graduate student, to improve its efficiency and versatility.¹¹ This polarizer performed exceptionally well and provided many experimental NMR results. However, it did possess certain limitations. Brass valves and copper tubing, over time, led to rather severe leaks, while the permanent silver-soldered connections made the accomplishment of a vast array of experiments difficult. This also made the addition of parts to the system and the replacement of leaking valves a complex situation.

Leaks are detrimental and harmful to a xenon polarizer. Rubidium is a highly reactive alkali-metal and will ignite upon reaction with the moisture in the atmosphere of a laboratory. This poses a major safety hazard making the achievement of a leak-tight apparatus a necessity. Even minute amounts of moisture can deactivate the rubidium within the pumping cell resulting in the loss of experiment time, as the pumping cell will then have to be laboriously cleaned, dried, and pressure tested before being loaded once again with rubidium. This loading process must take place inside of a glove box that is absent of moisture, a dangerous and often times stressful task where numerous safety precautions must be taken. Consequently, in the name of safety and experimentation time, it is best practice to develop a system that is completely free of leaks while at the same time functional with the ability to interchange parts should the need arise.

Polarizer Design/Construction

To accomplish this task, our polarizer was constructed solely out of stainless steel parts. Though costly, this offers the benefit of a longer life and better resistance to wear when compared to brass and copper parts. With the exception of the gas-recirculating pump, gas reservoir, solenoid valves, and flow controller, all of the parts used to construct the ^{129}Xe polarizer/gas handling system were purchased new. This made the accomplishment of a leak-tight system feasible.

Figure 3-1 represents our design for the gas handling system and polarizer. The red line indicates the flow path of xenon. Thermally-polarized xenon enters the pumping cell. Upon exiting the pumping cell, the xenon is hyperpolarized through SEOP and then travels through the NMR probe and sample that is inside of a superconducting magnet. It then travels through a flow controller which simultaneously indicates and regulates the gas flow. After that, it travels through a rotary-vane gas-recirculating pump that is capable of achieving both low and high pressures. It then proceeds through a moisture trap before again entering the pumping cell for re-hyperpolarization. The dashed-blue line indicates the aluminum table upon which the gas handling system was built. It should be noted that the pumping cell is contained inside of a hyperpolarization chamber and is not in the center of the table.

Several bypasses have been built into this system to allow for the easy activation of samples and testing of flow rates. These include bypasses for the moisture trap, the pumping cell, and the NMR probe/sample.

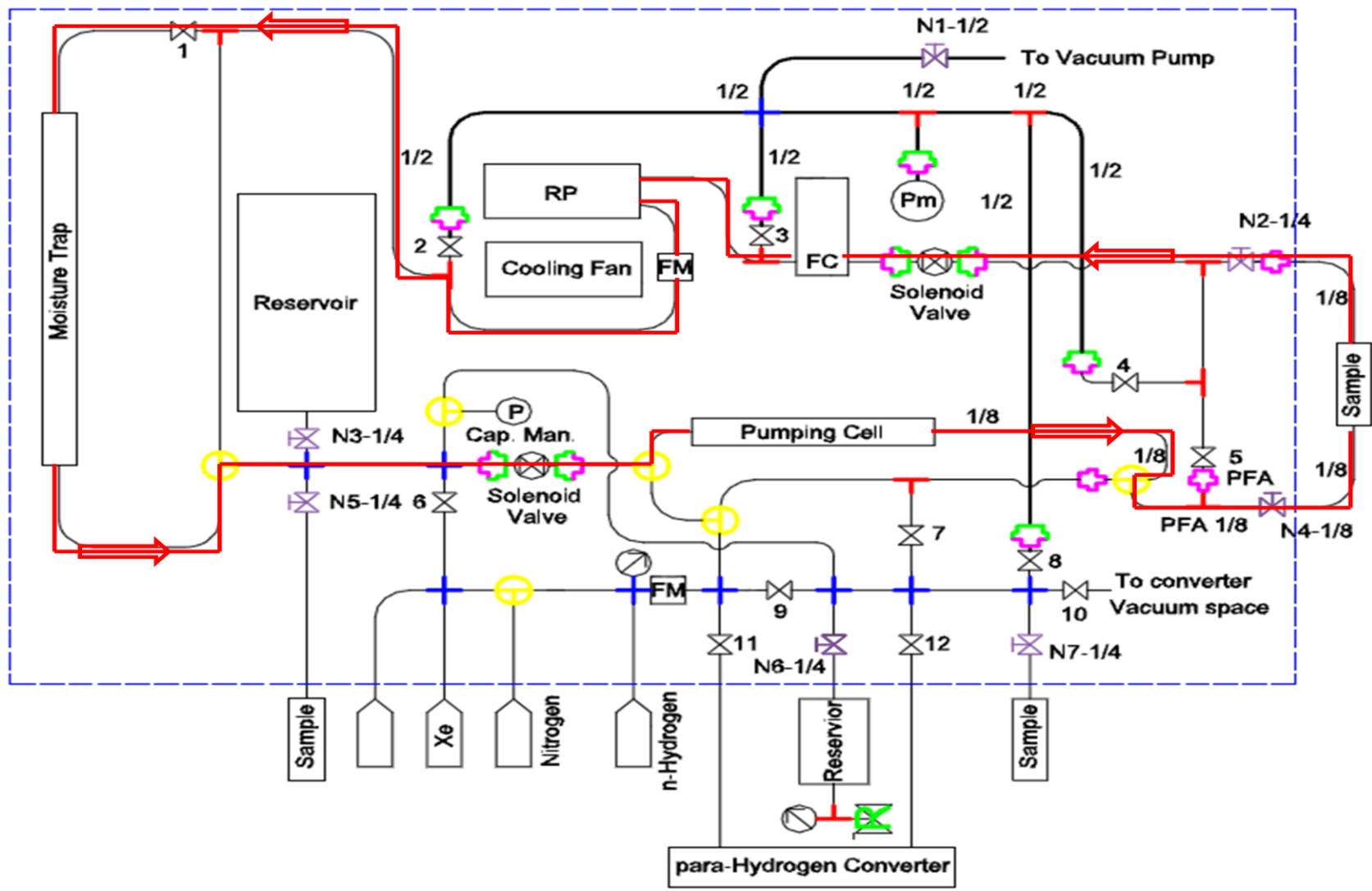


Figure 3-1. ^{129}Xe gas handling system and polarizer

Utilizing these bypasses, we have the ability to further activate a sample by passing xenon, nitrogen, or helium gas through the NMR probe/sample and the moisture trap while bypassing the rubidium inside of the pumping cell. When the sample has been sufficiently activated and dried, we can then pass xenon through the pumping cell and the NMR probe/sample while bypassing the moisture trap. This is done to prevent contamination within the moisture trap from reaching the rubidium.

Another benefit of these bypasses is that they allow the sample and system to be tested for leaks before exposure to the pumping cell and rubidium. As will soon be discussed, our sample holder is made of a plastic and achieving a leak-tight seal is not guaranteed. Accordingly, this must be checked before experiments can proceed.

These bypasses offer a sizeable advantage over the previous polarizer utilized by Zook and Cheng, while the utilization of all stainless steel parts should provide the gas handling system with leak resilience for an indefinite period of time.

Sample Holder

Our custom-designed sample holder is made from polyether ether ketone (PEEK). It features two hollow nuts that allow for 1/8" perfluoroalkoxy (PFA) tubing to transfer gas through the sample holder while maintaining a leak-tight seal utilizing PEEK flange-free ferrules. This is represented in Figure 3-2.



Figure 3-2. Top view of the NMR probe and sample holder. (Photo courtesy of author)

As can be seen in Figure 3-2, 1/8" PFA tubing travels up through the body of the probe. It then goes into the sample holder where a leak-tight seal between the tubing and the sample holder is created. From there, the xenon gas travels through the sample, which is packed into the narrower diameter of the sample holder and is surrounded by the radiofrequency (RF) coil. This RF coil attaches to two brass leads that sit atop the NMR probe. The sample is held in place by two glass wool plugs on each side of the sample. The sample is packed into the sample holder using a custom-machined tool that allows the sample to be packed around a brass rod that extends through the sample holder. This creates a path for the gas to travel through the sample and sample holder at flow rates that will allow for sufficient xenon polarization and subsequent NMR experiments. Upon exiting the sample holder, the gas travels back through 1/8" PFA tubing down the opposite side of the probe and exits through the bottom of the magnet where it is re-introduced to the ^{129}Xe polarizer.

Hyperpolarization Chamber

The most important and critical part of the ^{129}Xe polarizer is the hyperpolarization chamber. This is where the process of SEOP takes place to hyperpolarize the xenon. Accordingly, the highly-reactive rubidium metal is found here contained inside of the pumping cell, which can be seen in Figure 3-3. The inlet of the pumping cell, which is shown on the right side of Figure 3-3, is fitted with an Ace-threaded adapter allowing 1/4" PFA tubing to connect the pumping cell to the gas-handling system via a Swagelok connection. The outlet, seen on the left side of Figure 3-3, is fitted with an identical adapter that allows for 1/8" PFA tubing to connect the pumping cell and the NMR probe/sample. The reason for using tubing with a reduced diameter for xenon exiting the pumping cell is to transfer the hyperpolarized gas to the sample as quickly as

possible. This prevents loss of signal from relaxation. It should also be noted that care was taken to minimize stainless steel valves between the outlet of the pumping cell and the NMR probe, as this could also weaken the polarization. The bulb on the bottom of the pumping cell, pictured in the bottom-center of Figure 3-3, is where rubidium is stored. The rubidium is loaded into the pumping cell through the inlet stopcock in a nitrogen-filled glove box. This is normally done about twice per year depending on the use of the ^{129}Xe polarizer.



Figure 3-3. Optical pumping cell for SEOP. (Photo courtesy of author)

Once filled with approximately 0.5g of rubidium, the pumping cell is placed inside of the custom-designed oven, seen in Figure 3-4. This design allows the pumping cell to slide into the oven through the back via the two slits that were cut into the sides. Once the pumping cell is inside, two panels are screwed in place to cover the slits, as shown. Two end plates are also attached to the front and back of the oven via screws.

These end plates have a 3" borosilicate optical flat directly in the center of them to allow laser light to enter and exit the oven. Copper tubing enters through the bottom of the oven and makes a closed, uniform loop throughout the oven. Small holes were drilled into this coil to allow for an even distribution of warm air. This air is pre-heated outside of the oven to a set temperature depending on the laser power being used, as irradiation also provides additional heating. The air enters the closed loop of the coil and this pressure build-up evenly forces the air through the small holes, which in turn heats the oven. The holes were drilled in a manner that prevented direct heating of the pumping cell, as this could result in unneeded stress on the cell causing it to explode. The temperature of oven is normally kept between 130 and 140°C, and its legs are mounted to the laser table using two clamps.

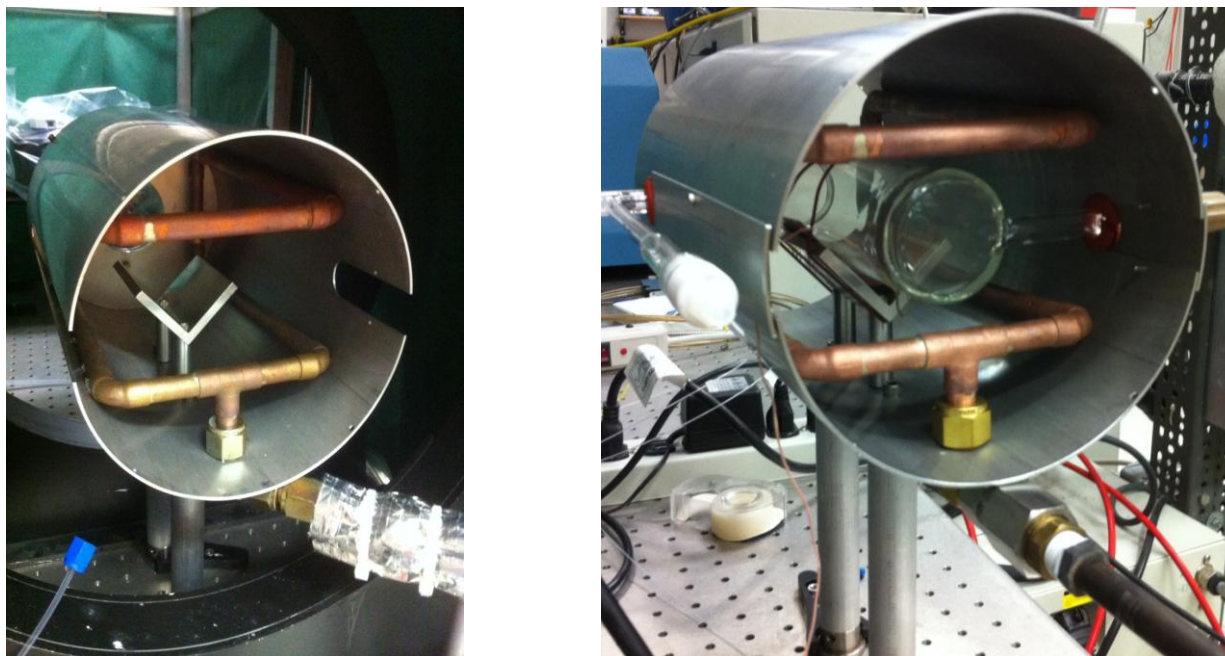


Figure 3-4. Oven constructed for SEOP (left) and the pumping cell placed inside of the oven (right). (Photos courtesy of author)

The oven is mounted to the laser table directly between a Helmholtz pair, which can be seen to the left of Figure 3-4. This pair consists of two circular magnetic coils

that are placed symmetrically on each side of the oven along a common axis. The coils possess an identical electrical current which flows in the same direction for both. These coils create a magnetic field surrounding the pumping cell of approximately 20 gauss which helps to create and retain the xenon polarization during gas circulation. The magnetic field of the pair is shown in Figure 3-5, where the homogenous region around 20 G represents the placement of the pumping cell.

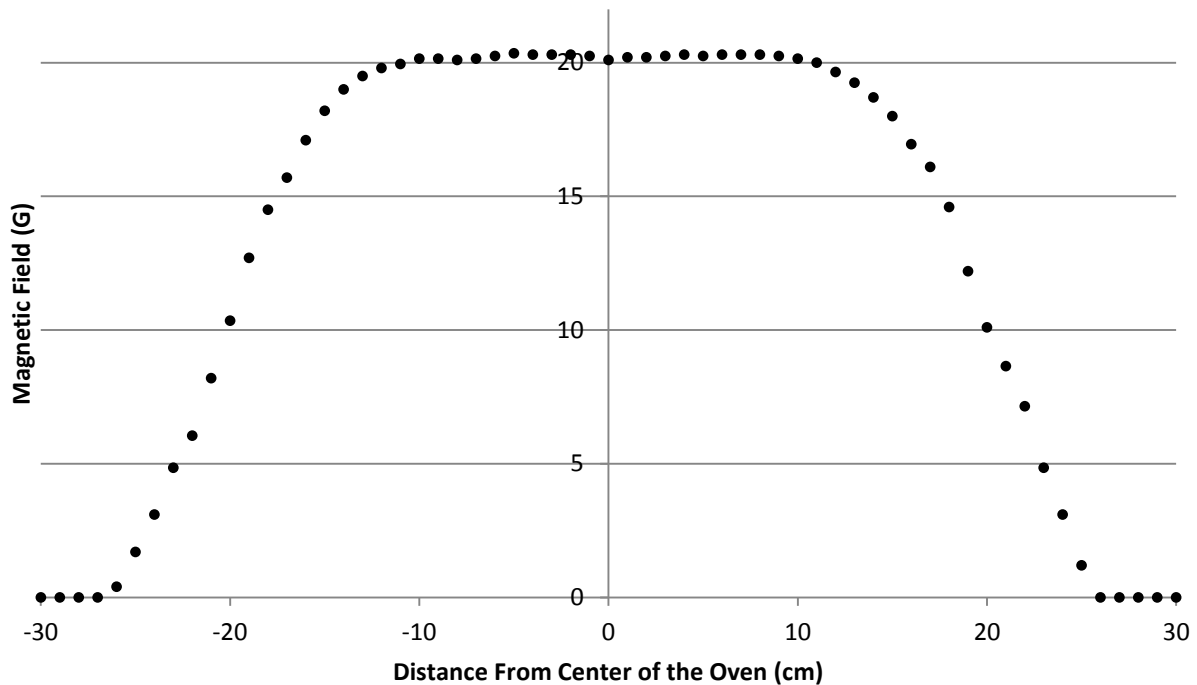


Figure 3-5. Magnetic field of Helmholtz coils

The final aspect of the hyperpolarization chamber is the fiber-optic coupled laser diode array. This allows for optical pumping of the rubidium inside of the pumping cell and oven through irradiation, which is seen in Figures 3-6 and 3-7. A laser trap is placed at the back window of the oven to catch any laser light that was not absorbed by the rubidium. This laser trap is cooled using a continuous, re-circulating flow of cold water to prevent excessive heating.

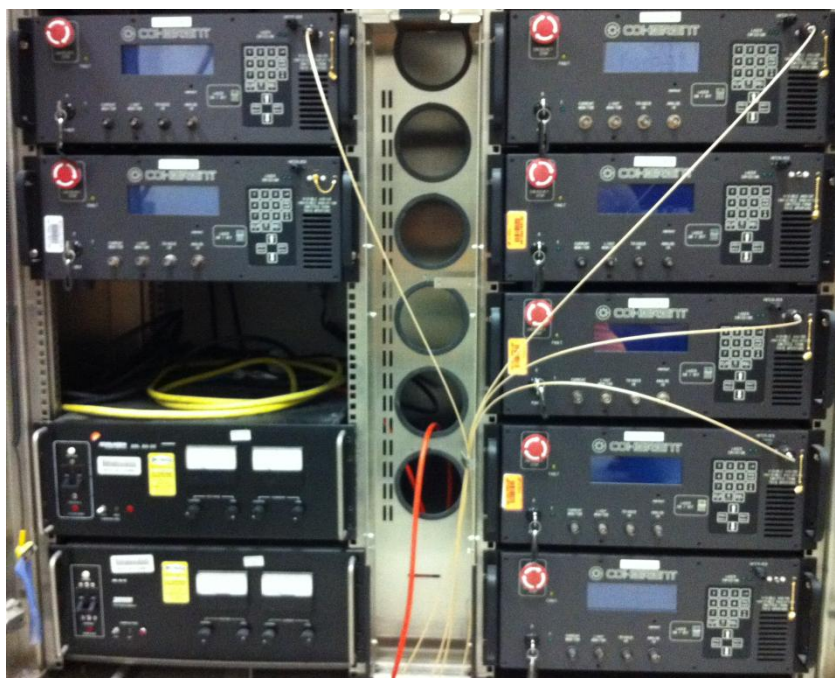


Figure 3-6 Fiber-optic coupled laser diode array. (Photo courtesy of author)

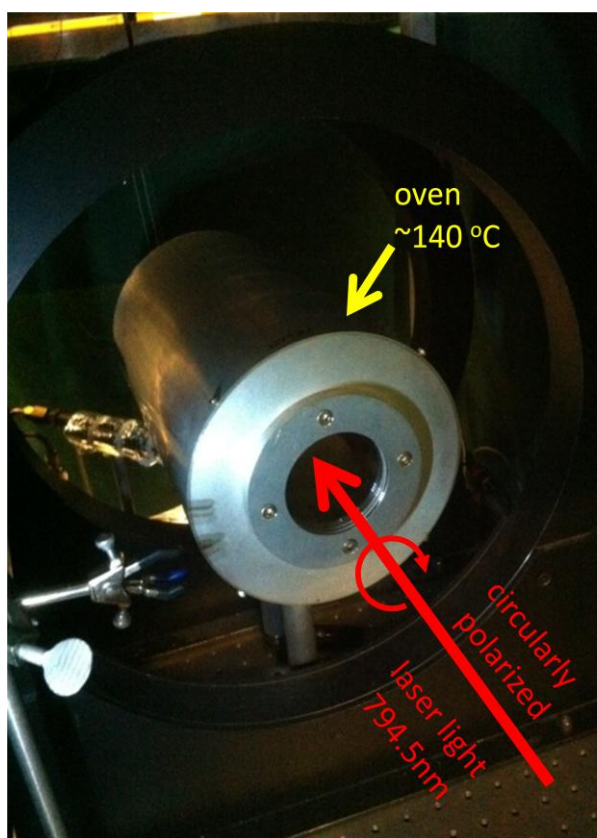


Figure 3-7. Fully-assembled oven in the hyperpolarization chamber. (Photo courtesy of author)

Upon exiting the hyperpolarization chamber, which is encased by aluminum and flame-retardant green laser curtains, the xenon quickly travels to the NMR probe/sample that is contained in the bore of the 9.4 Tesla superconducting magnet. The fully-assembled ^{129}Xe polarizer/gas-handling system is shown in Figure 3-8.

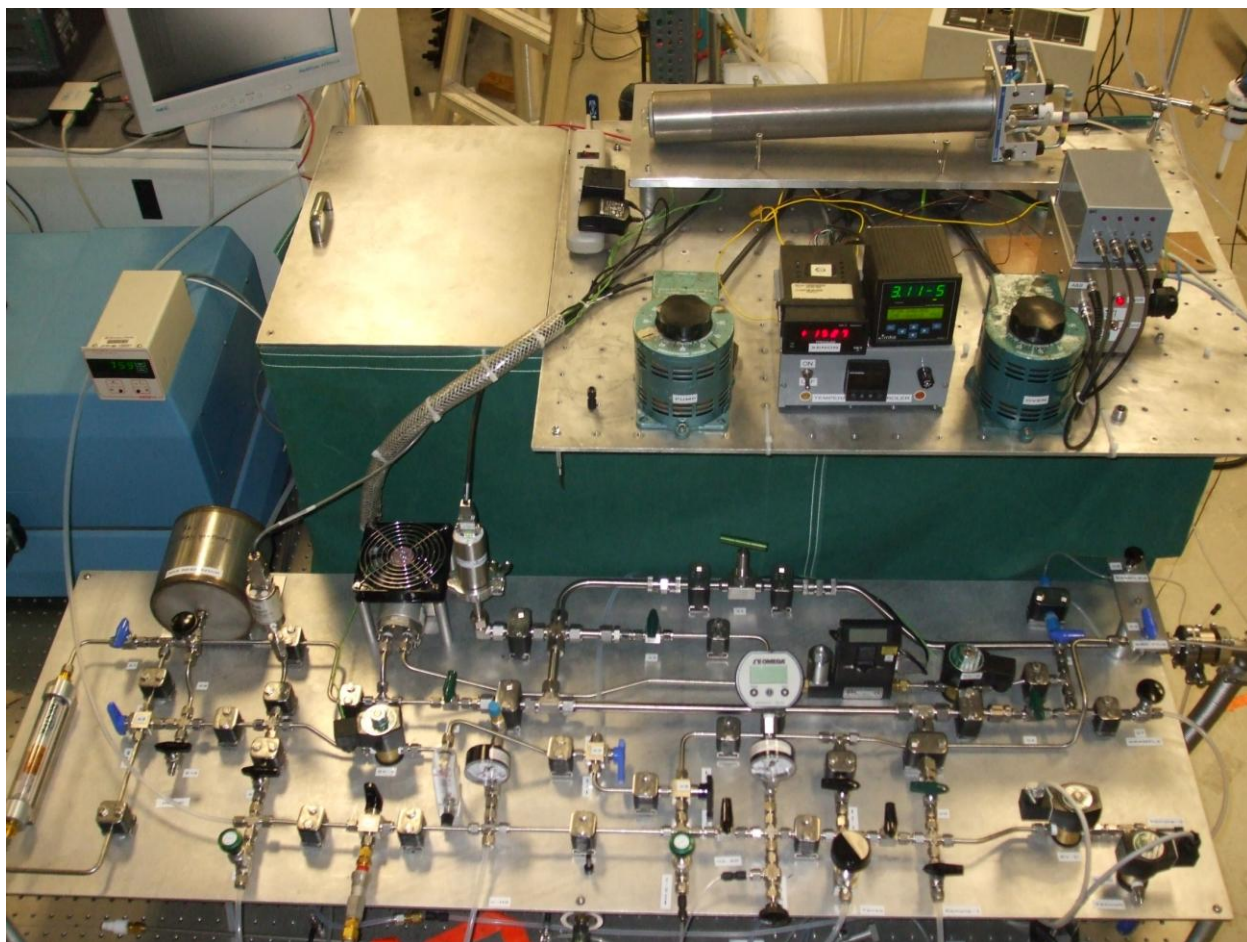


Figure 3-8. ^{129}Xe polarizer/gas-handling system. (Photo courtesy of author)

With this polarizer, NMR studies were conducted on two nanoporous materials which will now be discussed.

CHAPTER 4
NANOPOROUS MATERIALS

L-Phenylalanyl-L-Phenylalanine

L-phenylalanyl-L-phenylalanine (FF), shown in Figure 4-1, is a dipeptide that is the core-recognition motif of β -amyloid polypeptide and is associated with diseases such as Alzheimer's.²⁰ It is known to be capable of self-assembly upon crystallization. Due to the chemical and physical stability and rigidity of its nanotubes, FF has garnered attention in the nanotechnology world. To date, numerous promising applications of FF nanotubes have been explored and developed.

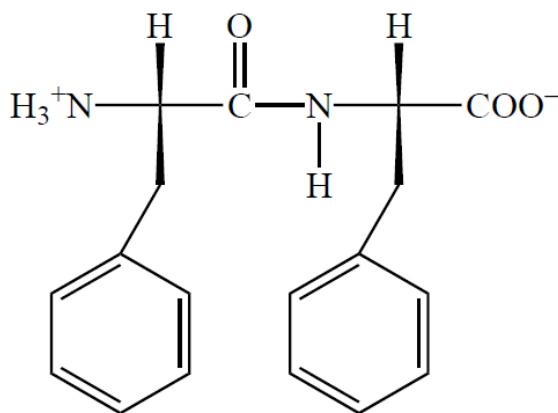


Figure 4-1. Schematic structure of FF. [Image reproduced with permission from Gorbitz, C.H. *European Journal of Chemistry* 2001, 7 (Page 5153). John Wiley and Sons.]

In 2003, Reches and Gazit reported the self-assembly of FF through the dilution of a concentrated solution of the dipeptide in 1,1,1,3,3,3-hexafluoro-2-propanol with water.²¹ Here, they showed that the stiff and discrete nanotubes that formed could serve as casts for the formation of silver nanowires possessing long, persistent lengths. This was performed through reduction of ionic silver within the FF nanotubes followed by enzymatic degradation of the peptide backbone.

Further investigations of FF nanotubes by Reches and Gazit have shown that they possess unique mechanical properties making them some of the stiffest biological materials currently known to exist.²² This was demonstrated and directly measured in 2005 through indentation type experiments using atomic force microscopy. These characteristics make FF attractive building blocks for the design and assembly of biocompatible nanodevices.

In 2004, synthesis of peptide-nanotube platinum-nanoparticle composites were reported using the D-phenylalanly-D-phenylalanine enantiomer.²³ This enantiomer is resistant to degradation by enzymes. Utilizing electron microscopy and Monte Carlo simulations, it was determined that the nanotubes were porous and were capable of forming the composites. This study also demonstrated an alternative to the crystallization method previously mentioned by Reches and Gazit which omitted the use of the 1,1,1,3,3,3-hexafluoro-2-propanol making the procedure more environmentally friendly. This crystallization method involved dissolving the dipeptide in water at an elevated temperature, waiting for equilibration, and then gradually cooling the sample to room temperature. This resulted in nanotubes that were 100nm to 2 μ m in diameter and in excess of 100 μ m in length.

In 2006, a study was performed investigating the chemical stability of FF nanotubes.²⁴ This involved mixing the nanotubes with numerous organic solutions including acetone, ethanol, acetonitrile, isopropanol, and methanol for approximately 30 minutes. These mixtures were then analyzed using scanning-electron microscopy which still revealed the assembled FF nanotubes. In addition to the remarkable

chemical stability reported, it was also demonstrated that the nanotubes possess extraordinary thermal stability at temperatures up to 90°C.

Gazit and Reches, in 2004, investigated the rationale behind the molecular self-assembly of FF nanotubes.²⁵ They hypothesized that one-dimensional propagation occurs through the linking of the dipeptides via hydrogen bonding. The inter-sheet stacking interaction that results between the aromatic groups of FF offers an energetic contribution to form extended β -sheets. The final tubular and nanoporous structure occurs through closure of the extended β -sheets along one axis, which is illustrated in Figure 4-2. This hypothesis is in agreement with other evidence found in 2005 which suggested the importance of FF groups in amyloid fibril formation through π - π stacking interactions.²⁶

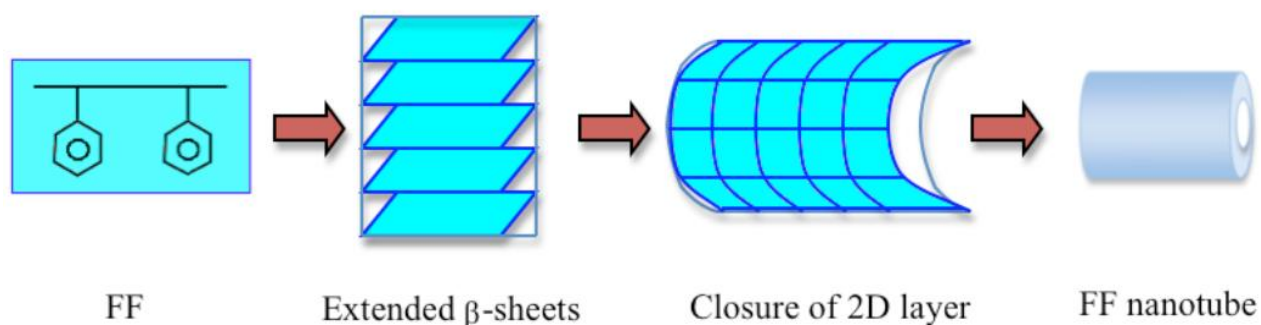


Figure 4-2. Model for the self-assembly of the FF nanotubes. [Image adapted with permission from Reches, M; Gazit, E. *Nano Letters* 2004, 4 (Page 584, Figure 5). American Chemical Society.]

In 2001, the molecular packing of FF nanotubes was investigated by Gorbitz.²⁷ Here, it was determined that the nanotubes have chiral hydrophilic channels with a van der Waals diameter of approximately 10Å, or 1nm. Within these hydrophilic channels, water molecules stay well organized, which is shown in Figure 4-3.

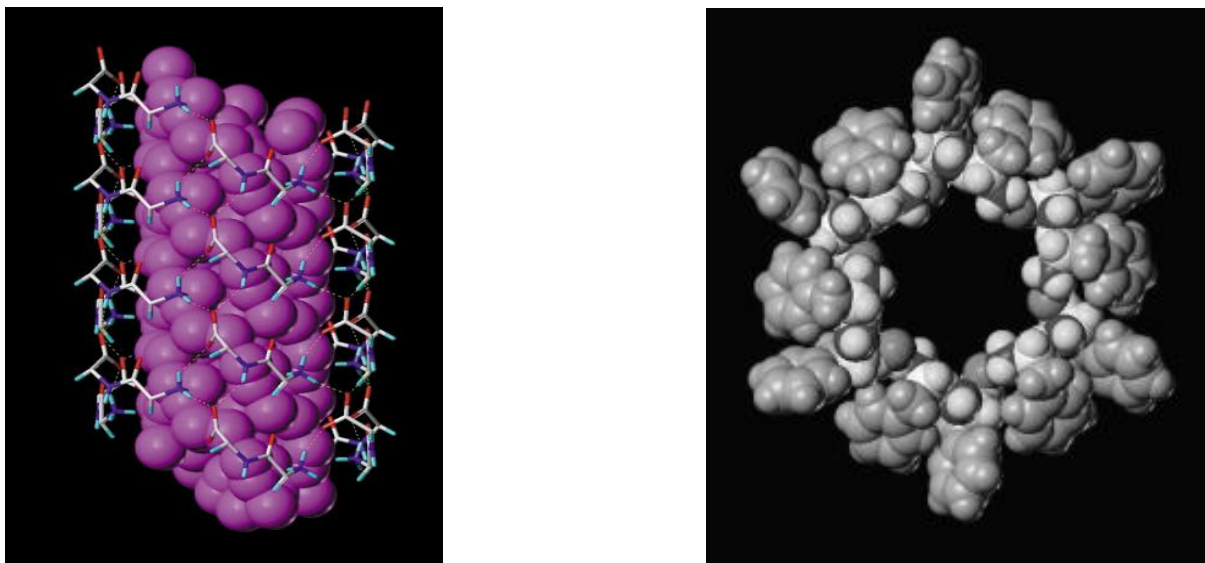


Figure 4-3. Channel of FF Nanotubes. Water positions inside a single channel (left), and a top view of the channel (right). [Image reproduced with permission from Gorbitz, C.H. *European Journal of Chemistry* 2001, 7 (Page 5157, Figures 4 and 5). John Wiley and Sons.]

These results were consistent with other results reported in 2004 where it was found that parallel channels ran in the direction of the FF tube axis.²³

In 2009, vertical alignment of FF nanotubes was achieved using vapor deposition methods.²⁸ This approach allowed the length and density of the nanotubes to be adjusted by cautiously controlling the supply of the building blocks from the gas phase. It was further shown that these nanotube arrays could be used to develop high surface area electrodes for energy storage applications, microfluidic chips, and highly hydrophobic self-cleaning surfaces. In another study, vertical alignment was attained by using a thin film of FF. Here, the dipeptide was dissolved in 1,1,1,3,3,3-hexafluoro-2-propanol in the absence of water to produce an amorphous peptide thin film. This film acted as a template and, under the proper conditions, FF nanorods grew.²⁹

In 2006, Reches and Gazit developed methods for horizontally and vertically aligning FF nanotubes.³⁰ Vertical alignment was achieved through axial unidirectional

growth of a dense array of the dipeptide. Horizontal alignment was attained through a non-covalent coating of the nanotubes with a ferrofluid and the application of an external magnetic field, which can be seen schematically in Figure 4-4.

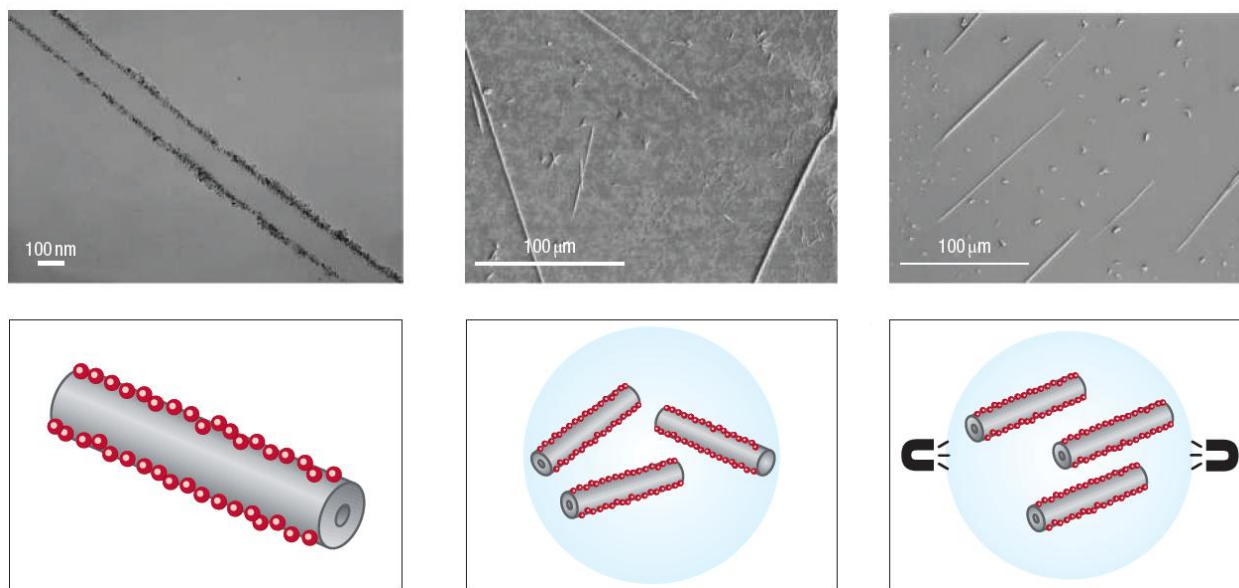


Figure 4-4. Self-assembled FF nanotubes coated with magnetic particles (left), coated nanotubes before exposure to an external magnetic field (center), and horizontally-aligned coated nanotubes after exposure to an external magnetic field (right). [Image reproduced with permission from Reches, M.; Gazit, E. *Nature Nanotechnology* 2006, 1 (Page 198, Figure 4). Nature Publishing Group.]

For the experiments and results presented in this thesis, the lyophilized form of FF was purchased from MP Biomedicals and was used as purchased. Some attempts were made to re-crystallize the FF utilizing the method of Reches and Gazit which involved an environmentally-hazardous solvent, but it was ultimately determined through scanning electron microscopy (SEM) that the dipeptide, as purchased, possessed adequate nanochannels for ^{129}Xe NMR studies. Figure 4-5 represents SEM images of the purchased FF that was utilized throughout these studies.

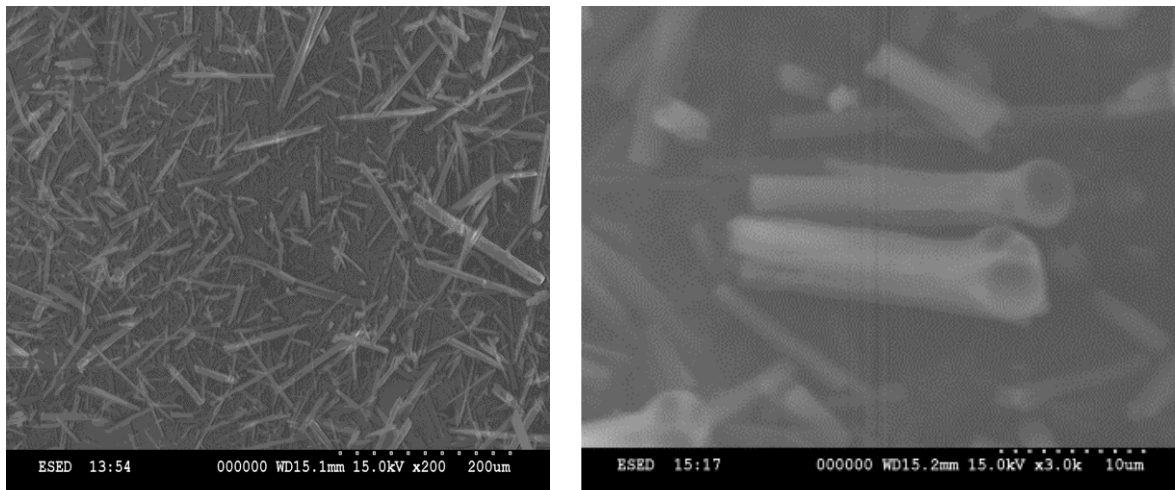


Figure 4-5. SEM images of FF showing the size distribution (left) and the actual nanochannel (right)

Bis-Urea Macrocycle

As mentioned previously, hollow nanotubular structures have a wide range of applications in biology, chemistry, and material science. As was seen with FF, there is great interest in the development of new molecular building blocks that predictably self-assemble into nanotubular structures. Accordingly, in 2001, a series of bis-urea macrocycles that are readily synthetically accessible and self-assemble into columnar nanotubes was designed.³¹

Bis-urea macrocycle 1, as referred to in the literature, was chosen for the present NMR studies and can be seen in Figure 4-6. Like FF, this macrocycle self-assembles into nanotubes. This self assembly process is guided primarily by hydrogen bonding and aromatic stacking interactions that yield crystals of filled host 1•acetic acid.³² These acetic acid guest molecules are bound in the cylindrical cavities of the bis-urea crystal. They can be removed through heating to form a stable crystalline apohost 1.

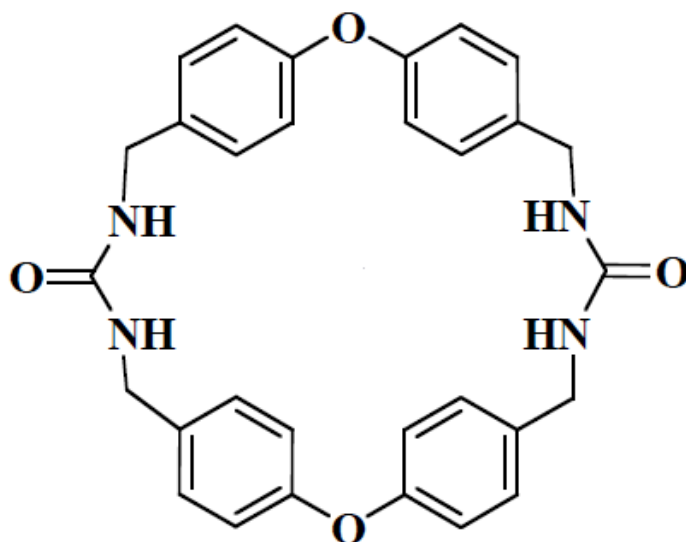


Figure 4-6. Bis-urea macrocycle 1.

This apohost possessed a type 1 carbon dioxide gas adsorption isotherm which is consistent with an open framework microporous material. It is able to bind a range of small-molecule guests with explicit stoichiometry. Similar to zeolites, apohost 1 can be reused because the formation of these inclusion complexes does little to destroy the crystal framework.

The nanochannels formed by bis-urea macrocycle 1 have an elliptical shape. The diameter of these nanochannels is approximately $3.7\text{\AA} \times 4.8\text{\AA}$.³² ^{129}Xe NMR has not previously been reported in the literature on any bis-urea macrocycles.

^{129}Xe possesses a collision diameter of approximately 4.4\AA .² As demonstrated in Figure 4-7, ^{129}Xe adsorption into the channels of bis-urea macrocycle 1 is not favorable given the dimensions of the nanochannels. Nevertheless, and as will be discussed shortly, xenon adsorption into the channels does occur.

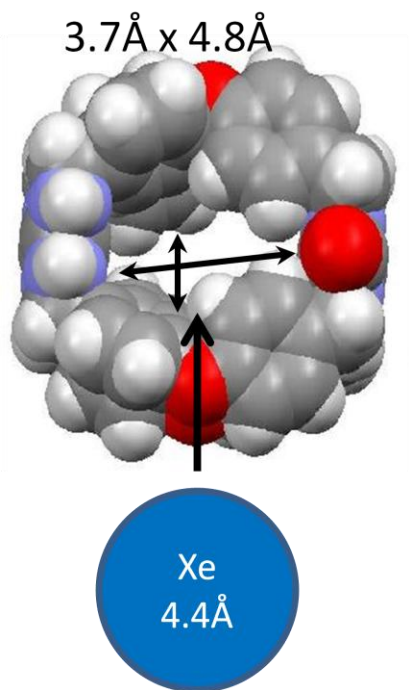


Figure 4-7. Illustration of xenon adsorption into the bis-urea macrocycle 1 nanochannels. [Image adapted with permission from Dewal, M.B.; Lufaso, M.W.; Hughes, A.D.; Samuel, S.A.; Pellechia, P.; Shimizu, L.S. *Chemistry of Materials* 2006, 18 (Page 4861, Figure 8). American Chemical Society.]

CHAPTER 5
METHODS AND PULSE SEQUENCES

Spin (Hahn) Echo

In NMR, the refocusing of magnetization utilizing a pulse of resonant electromagnetic radiation is referred to as a spin echo. The spin echo pulse sequence is depicted below in Figure 5-1. It was discovered in 1950 by Erwin Hahn and was further developed by Carr and Purcell.^{33,34}

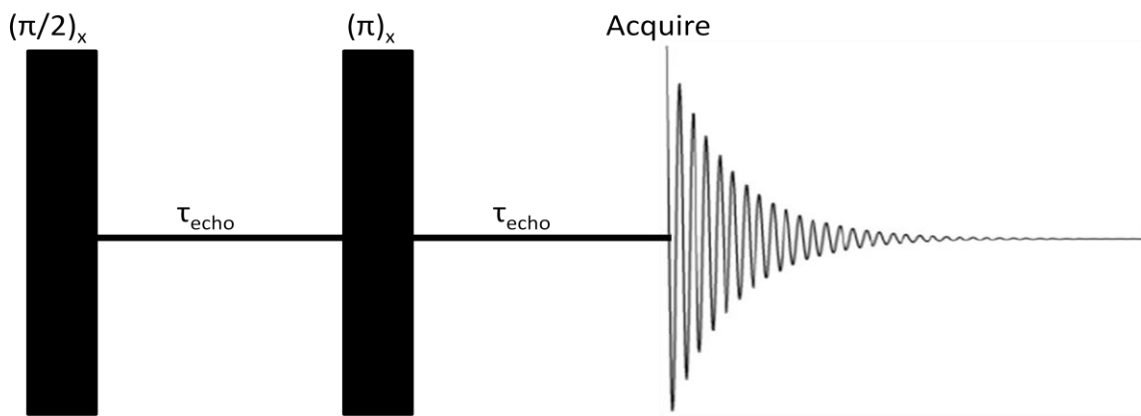


Figure 5-1. Spin (Hahn) echo pulse sequence

The observable NMR signal following an initial excitation pulse decays with time due to spin relaxation and inhomogeneous effects. These inhomogeneous effects cause different spins within a sample to precess at different rates.³⁵ Spin relaxation leads to a loss of magnetization that is irreversible. However, inhomogeneous effects such as a magnetic field gradient or a distribution of chemical shifts can be removed by applying a π pulse which inverts the magnetization vectors. If this inversion pulse is applied after a time τ of dephasing, the inhomogeneous evolution will rephrase to form an echo at time 2τ . At this time, the chemical shift and field inhomogeneity are refocused leading to a truer representation of the actual NMR signal.

This pulse sequence was utilized for the temperature dependence study of FF nanotubes. The experimental parameters included a recycle delay of 5s, a pressure of approximately 2300 Torr, a gas flow-rate of about 250mL/min, and 128 scans. With the exception of the inversion and saturation recovery experiments, all of the data collected for this thesis were done on a Bruker 400MHz Avance spectrometer.

Hyperpolarized ^{129}Xe Tracer-Exchange

The tracer-exchange method can be used to study the diffusion time-scaling over a wide range of time-scales, from approximately 10ms to 1000s. The experiment begins with the destruction of the spin polarization of xenon atoms inside of the nanochannels and is then followed by measurement of the recovery of the polarization as a function of time. At time $t = 0$, there is no signal, as the spin polarization of the xenon atoms inside of the channel has been saturated. As t increases, however, the hyperpolarized xenon atoms outside of the channels exchange with the unpolarized atoms inside of the channels leading to the observation of an NMR signal growing in due to the “exchanged” hyperpolarized atoms. At sufficiently long t values, the hyperpolarization distribution reaches a steady-state, resulting in the maximum observable NMR signal. This is depicted graphically in Figure 5-2.

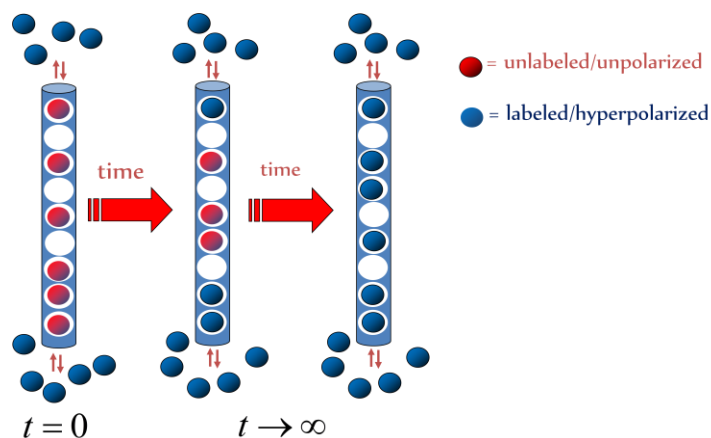


Figure 5-2. Illustration of the hyperpolarized NMR tracer-exchange

To achieve saturation at time $t = 0$, a train of selectively-saturating pulses is applied to destroy the polarization inside of the nanochannels. A certain amount of time then passes which allows hyperpolarized atoms outside of the channels to exchange with the unpolarized atoms inside of the channel. Once that time has passed, an acquisition pulse is applied and the NMR signal is collected. This is represented in the pulse sequence of Figure 5-3.

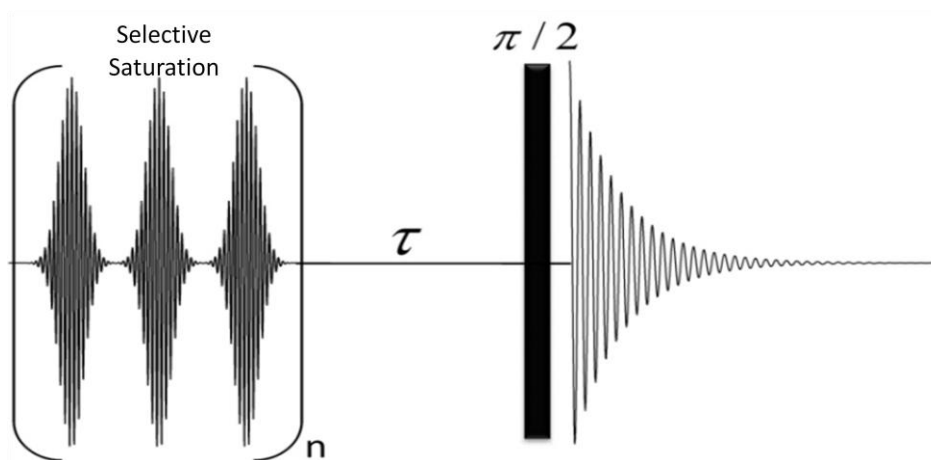


Figure 5-3. Tracer-exchange/selective saturation recovery pulse sequence

This method was first demonstrated in 2000, where xenon diffusion inside tris (o-phenylenedioxy) cyclotriphosphazene, or TPP, nanochannels was measured with respect to time as a function of temperature and occupancy utilizing continuous-flow hyperpolarized ^{129}Xe saturation-recovery NMR.³⁶ These experiments made use of non-selective saturating pulses which destroyed all of the xenon magnetization inside of the sample space. The recovery of the xenon signal inside of the channels was monitored as a function of diffusion time under continuous-flow conditions. This use of non-selective saturating pulses creates an ill-defined initial condition for the magnetization kinetics modeling.

A well-defined initial condition is obtained by using frequency selective saturating RF pulses, which was demonstrated in 2007 by Cheng and Bowers.³⁷ This makes it possible to destroy the xenon magnetization inside of the nanochannels while leaving the magnetization of the xenon bulk gas phase unaffected. The selective-saturation recovery pulse sequence has been employed throughout the studies contained in this thesis. The tracer exchange curve, $\gamma(t)$, can be defined as:

$$\gamma_{nmr}(\tau) = \frac{signal_{\tau}}{signal_{\tau \rightarrow \infty}} \quad (5-1)$$

As demonstrated in the literature, this tracer exchange curve can be used to distinguish between single-file diffusion (SFD) and normal diffusion (ND) in nanotubular materials.³⁶⁻³⁸ Single-file diffusion occurs when the atoms inside of the channel are unable to pass one another. When this happens, the mean-squared displacement is proportional to the square-root of the observation time:

$$\langle \Delta z^2(t) \rangle = 2F\sqrt{t} \quad (5-2)$$

Here, F is the single-file mobility. Normal diffusion occurs when the atoms inside of the channel can pass one another. This results in a mean-squared displacement that is proportional to the observation time,

$$\langle \Delta z^2(t) \rangle = 2Dt \quad (5-3)$$

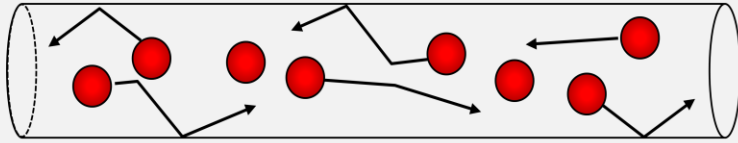
Here, D is the diffusivity. These two modes of diffusion are illustrated in Figure 5-4.

The tracer-exchange fitting functions for SFD and ND are shown in Equations (5-4) and (5-5), respectively.³⁷

$$\gamma_{nmr}^{SFD}(\tau) = \frac{1}{\Gamma(1/4)T_{1c}^{1/4}} \int_0^{\tau} t^{-3/4} e^{-t/T_{1c}} dt \quad (5-4)$$

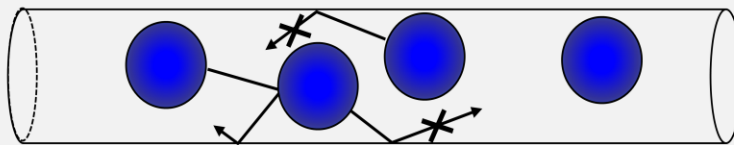
$$\gamma_{nmr}^{ND}(\tau) = \frac{1}{(\pi T_{1c})} \int_0^{\tau} t^{-1/2} e^{-t/T_{1c}} dt \quad (5-5)$$

Normal Diffusion (ND)



$$\langle \Delta z^2(t) \rangle = 2Dt$$

Single-File Diffusion (SFD): molecules *cannot* pass



$$\langle \Delta z^2(t) \rangle = 2F\sqrt{t}$$

Figure 5-4. Single and normal file diffusion in 1D channels

In these functions, T_{1c} is a fitting parameter and represents the spin-lattice relaxation time of the tracer inside the channels.

Inversion Recovery

In NMR, the time constant T_1 is referred to as the spin-lattice relaxation time, or longitudinal relaxation time. It represents the time to reestablish the thermal equilibrium Boltzmann distribution following a perturbation. The T_1 inversion recovery experiment is a common method for measuring this time constant.

In the inversion recovery pulse sequence, shown in Figure 5-5, the magnetization, M_0 , is initially inverted with a π pulse. Following this is a time τ which allows for relaxation along the $+z$ -axis. After this time τ has passed, the NMR signal is measured by applying a $\pi/2$ pulse.

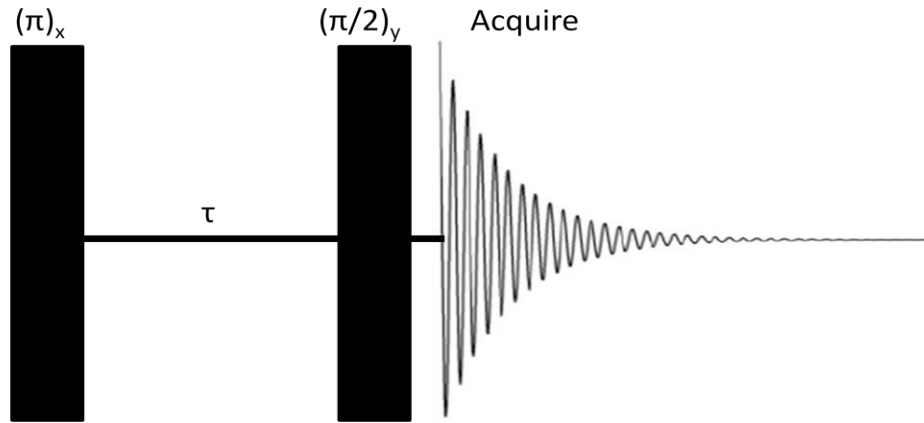


Figure 5-5. Inversion recovery pulse sequence

Utilizing the method, the longitudinal relaxation time constant can be determined by fitting the magnetization curve using the following function:⁹

$$M = M_0(1 - 2e^{-\tau/T_1}) \quad (5-6)$$

Alternatively, T_1 can be directly calculated utilizing the following formula, where τ_n is the τ corresponding to the node at $M = 0$:

$$T_1 = \frac{\tau_n}{\ln(2)} \quad (5-7)$$

Another technique that is sometimes used to measure T_1 relaxation is the saturation recovery method.

Saturation Recovery

In the saturation recovery method for the measurement of the longitudinal relaxation, any initial magnetization present in the beginning of the experiment is destroyed using a train of $\pi/2$ pulses. Longitudinal magnetization then accumulates for a time τ . It is then converted into detectable transverse magnetization using a $\pi/2$ pulse and the NMR signal is acquired. This is shown in the pulse sequence of Figure 5-6. The NMR signal represents the recovery of the longitudinal magnetization back towards its thermal equilibrium value of M_0 as a function of τ .

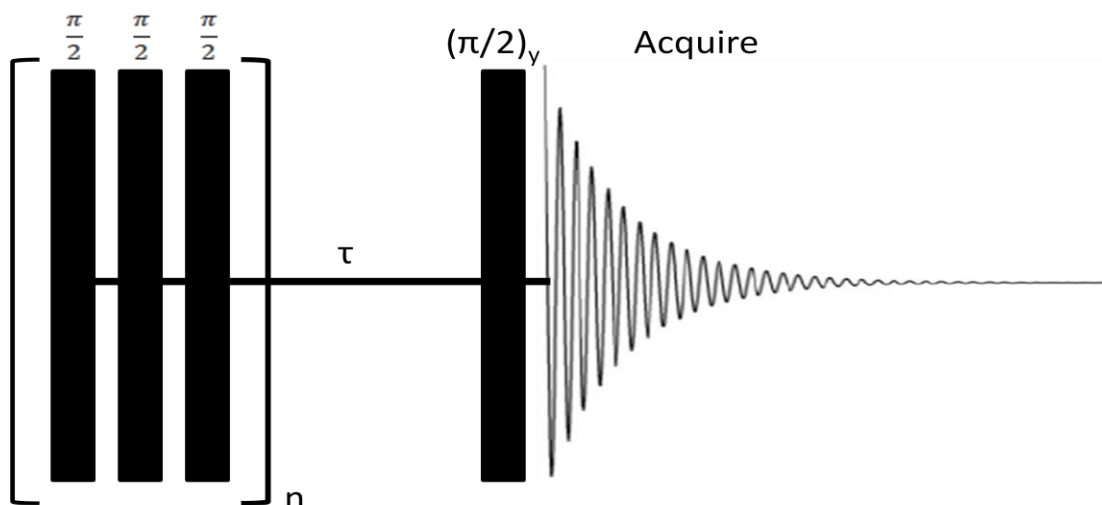


Figure 5-6. Saturation recovery pulse sequence

The saturation recovery pulse sequence is similar to the tracer-exchange experiment with the exception being that all magnetization is initially saturated rather than only magnetization in a specific environment. Besides this initial difference in the type of pulse used to destroy the magnetization, the two are identical.

A major advantage of using the saturation recovery method over the inversion recovery method to measure T_1 relaxation is that no recycle delays have to be included between scans. This makes signal averaging much more cost effective with saturation recovery by drastically decreasing the experiment time, especially in samples with rather long T_1 values.

Using saturation recovery, T_1 can be determined by fitting the magnetization curve using the following function:⁴⁰

$$M = M_0(1 - e^{-\tau/T_1}) \quad (5-8)$$

The inversion and saturation recovery experiments were carried out on a Varian Inova 500MHz spectrometer.

CHAPTER 6 RESULTS AND DISCUSSION

L-Pheynyalanyl-L-Pheynlalanine

Xenon Adsorption at Various Temperatures

The first study performed on FF included a variable temperature study using the spin echo pulse sequence mentioned previously. The FF nanotubes contain two channels of different sizes. Each of these channels gives rise to a distinct NMR signal, as seen in the variable temperature study. The large central channels of crystalline FF have diameters ranging from 100 to 300nm.²⁰ The exact nature of this inner surface is not known, but it is believed to be either mixed hydrophobic/hydrophilic, or entirely hydrophobic. The smaller, individual, and narrow channels of FF make up the dipeptide wall. The diameters of these channels are approximately 10Å, or 1nm. These channels are hydrophilic in nature and have the ability to accommodate guest molecules of some size.

The temperature study that was carried out on the FF nanotubes utilizing a Bruker Avance 400MHz spectrometer is shown in Figure 6-1. These were hyperpolarized ¹²⁹Xe spin echo variable temperature experiments using pure natural-abundance xenon gas. Spectra were acquired at temperatures ranging from room temperature to -96°C. At temperatures greater than -75°C, only two peaks are observed and those spectra have been omitted from Figure 6-1. However, as the temperature is decreased below -75°C, a third peak begins to grow in around 240ppm. The intensity of this peak continues to increase with decreasing temperature at the expense of the intensity of the middle peak, which is centered around 60ppm. This peak around 240ppm represents xenon adsorption into the small, 1nm channels while the broad peak close to 60ppm

represents xenon adsorption into the large, central channel. The narrow peak close to 0ppm represents the bulk xenon gas, which was referenced to 0ppm at 25°C.

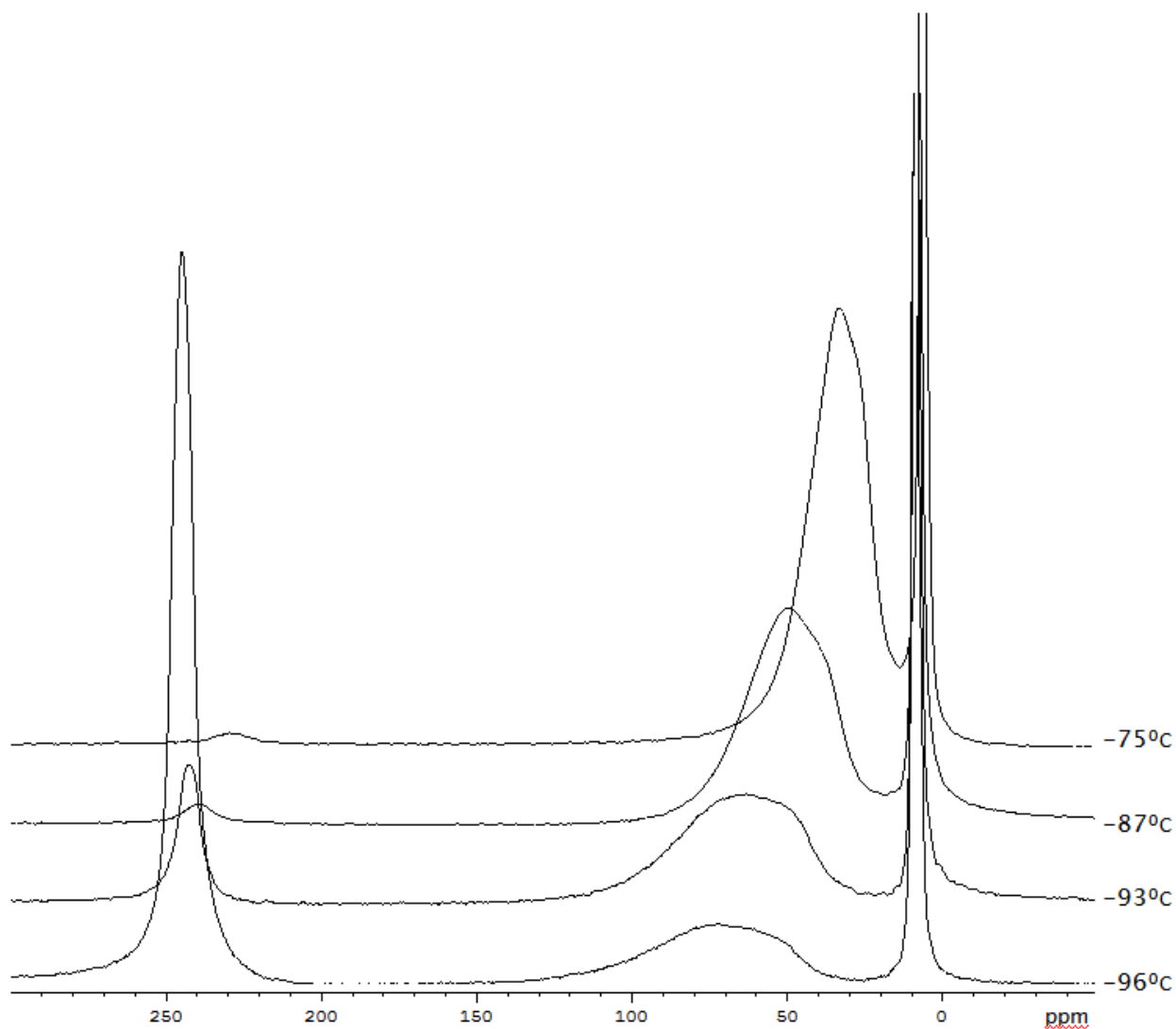


Figure 6-1. Variable temperature hyperpolarized ^{129}Xe study on FF nanotubes utilizing the spin-echo pulse sequence with 128 scans and a recycle delay of 5s.

These results indicate a temperature dependence of the adsorbed xenon chemical shift. The chemical shift of both phases decreases with increasing temperature. This is in agreement with a study performed in 1995 which analyzed the temperature dependence of the xenon chemical shifts in other microporous solids.⁴¹ Here, it was determined that the chemical shift is sensitive to the shape of the potential experienced

by the xenon atom inside of the pore. It was found that if the pore is about the same size as the xenon atom, then the potential has a single minimum around the center of the pore. This, in turn, leads to a chemical shift that increases with temperature.⁴¹ However, for larger pores, as is the case with FF nanotubes, the potential has a hump near the center which is surrounded by a low-energy trough. In this type of system, the xenon chemical shift decreases with increasing temperature, which represents the trend seen in Figure 6-1.

These results also show that at decreasing temperatures, xenon redistributes from the large, central channel to the small, narrow channels making up the wall of FF. This is evidenced by the decreasing signal at 60ppm and the increasing signal at 240ppm as the temperature is decreased. The intensity of the bulk xenon gas peak remains unchanged as the two adsorbed peaks undergo exchange. To further probe the xenon diffusion through these two channels, the tracer-exchange method was employed.

Tracer-Exchange

The adsorption of Xe into the small channels of FF at -93°C was chosen for the tracer-exchange experiments. The spectra for these experiments, acquired as a function of time, are shown in Figure 6-2.

The experiments were carried out with τ values ranging from 0.1ms – 200s. However, after about 5s, the hyperpolarized xenon steady-state was re-achieved. Figure 6-2 shows the recovery of the polarization from 0-6s.

The integrals of the signals arising from the adsorption into the two different channels were referenced to the bulk xenon gas peak. This was done because the bulk xenon peak fluctuated very little and remained essentially constant throughout the experiments. The integrals were normalized to an average of the τ_{∞} value which

corresponds to the hyperpolarized steady-state. These values were then fitted to the tracer-exchange fitting functions described in Equations (5-4) and (5-5).

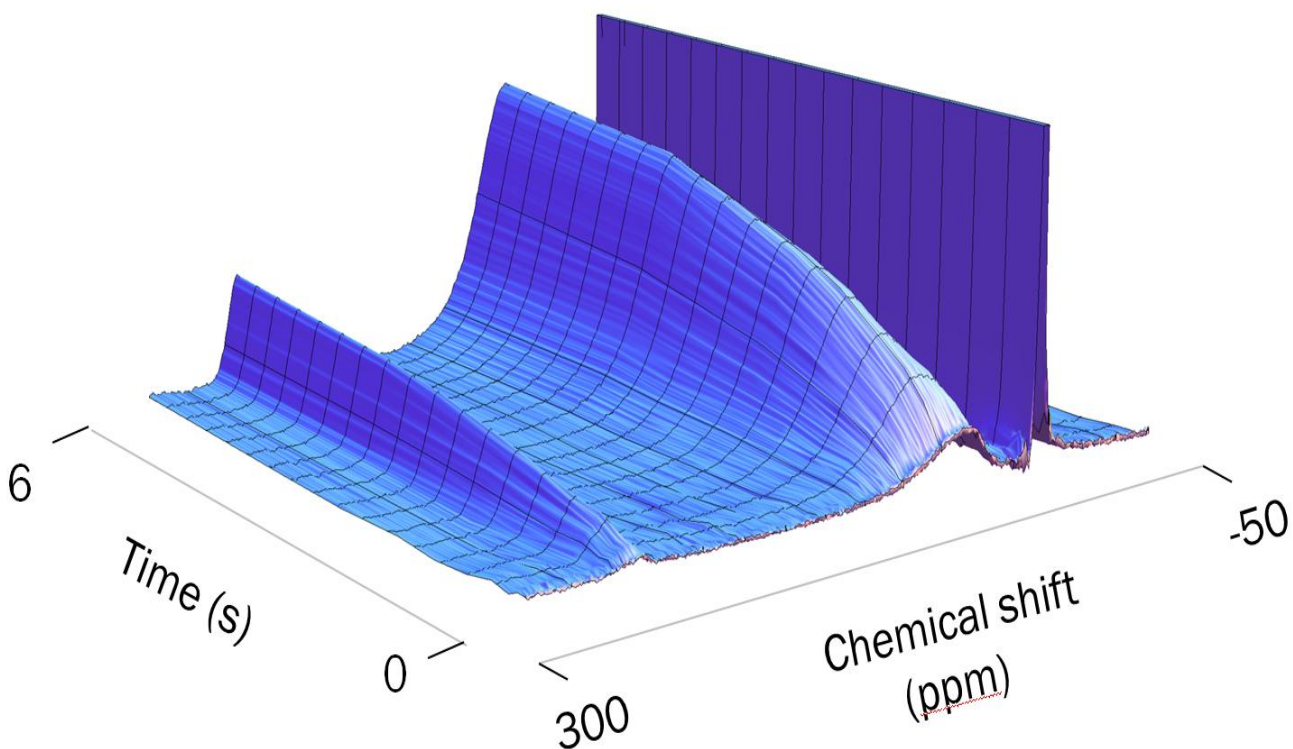


Figure 6-2. Tracer-exchange data on FF nanotubes

As seen in Figures 6-3 and 6-4, both the small and large channels of FF show a very reasonable fit to the NMR tracer-exchange function (Eq. [5-5]) for normal diffusion. This is expected given the channel diameters. The small, narrow channel possesses a diameter of 10\AA which allows for two xenon atoms to pass one another inside of the channel. This is even more the case for the larger-diameter channel. The longitudinal relaxation times extracted from these fits for the small and large channels were 5.4s and 3.6s, respectively.

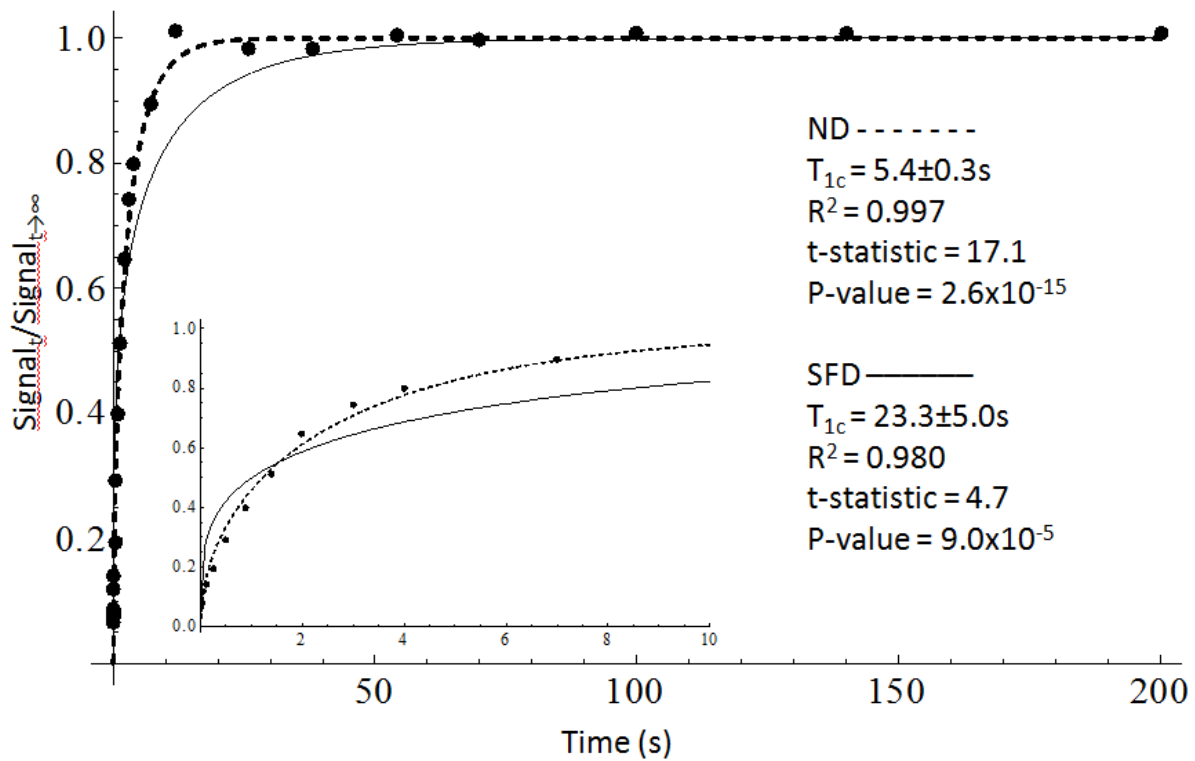


Figure 6-3. Tracer-exchange fits to the small, 1nm channels of FF

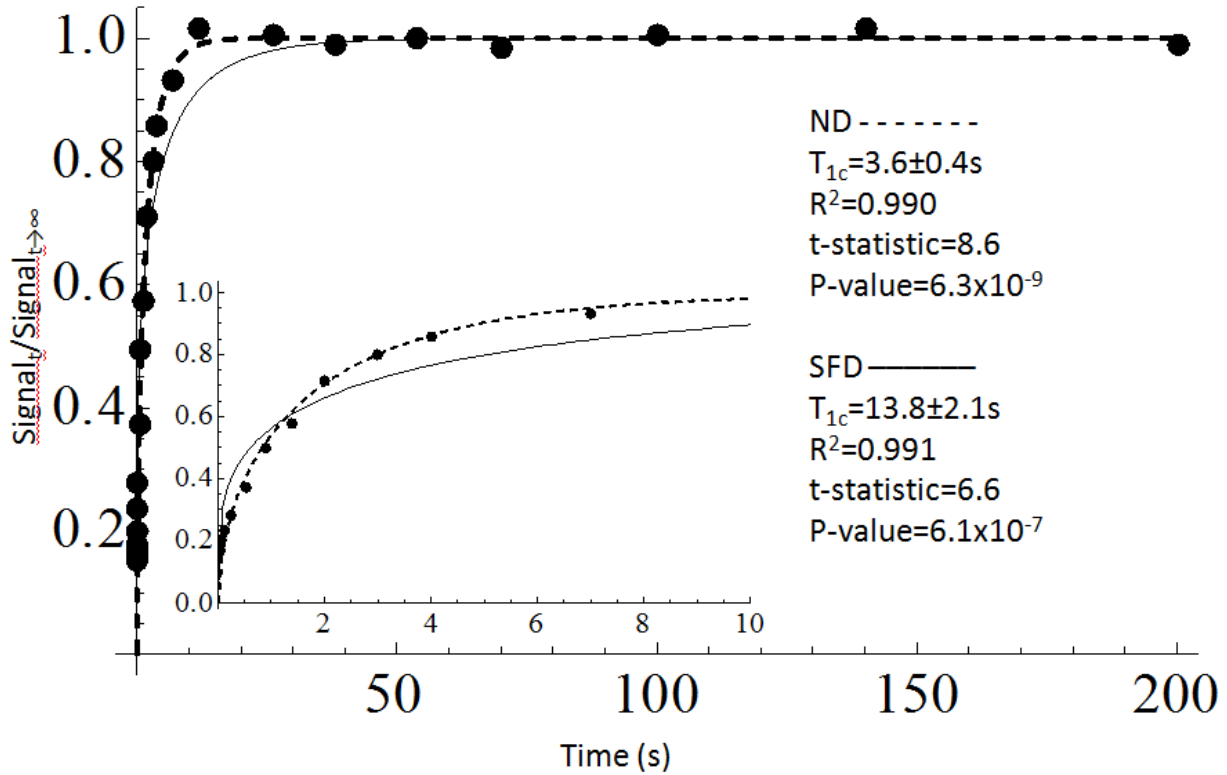


Figure 6-4. Tracer-exchange fits to the large, central channels of FF

T₁ Estimation

In an attempt to verify the T₁ values that were extracted from the tracer-exchange fitting functions, thermally-polarized ¹²⁹Xe saturation recovery experiments were performed on FF on a Varian Inova 500MHz spectrometer at a similar pressure to the tracer-exchange experiments. Similar experiments were performed on a xenon gas reference sample consisting of 10 bar pure xenon gas and 1 bar oxygen. Also performed on this reference sample were inversion recovery experiments to verify the T₁ values obtained from the saturation recovery experiments.

The FF sample was cooled to -85°C where xenon adsorption into both channels was observed. This made it difficult to verify the T₁ values extracted from the tracer exchange fitting functions, as the experiments were performed at two different temperatures. This difference in temperatures was not intentional and was realized only after a calibration of the variable temperature apparatus used for the hyperpolarized experiments was performed, as this was done after all data had been collected.

Also of concern here, however, is the fact that during the hyperpolarized experiments, warm gas is flowing through the sample and sample holder while the thermocouple measuring the temperature of the sample is outside of the sample holder barely extending out through the probe-head. This investigation of the effect that the circulation of warm gas has on the temperature is a continuing investigation. It is believed that the temperatures reported in the hyperpolarized xenon variable temperature and tracer exchange experiments may actually be higher due to the warming effects of the gas flow. Once these things are resolved and it is known with certainty what the temperature of the sample is when hyperpolarized experiments are

conducted, the T_1 relaxation values can be compared to the values obtained from the thermally-polarized xenon inversion and saturation recovery experiments. Because the thermally-polarized experiments were carried out on sealed samples using a different spectrometer which had a different variable temperature setup that was calibrated to the splitting of methanol, the accuracy of the temperatures for those experiments is unquestionable.

As just mentioned, T_1 saturation and inversion recovery experiments were performed on a xenon reference sample. This was done to ensure continuity between the two different methods for measuring T_1 . The inversion recovery and saturation recovery experiments for the reference sample at room temperature are shown in Figures 6-5 and 6-6, respectively. The same experiments at -85°C are shown in Figures 6-7 and 6-8, respectively.

The absolute integrals of the signal were tabulated, normalized to the value corresponding to the maximum integral/signal, and plotted with respect to the recovery time. As can be seen in Figures 6-5 – 6-8, the two different methods for measuring the longitudinal relaxation give roughly the same values that are within the experimental errors of each other. Being that the FF experiments needed to be performed at temperatures well below room temperature, similar experiments were performed on the xenon gas reference sample at -85°C . This was done simply to ensure consistency between the results and also to reference the bulk xenon gas peak to 0ppm at that specific temperature.

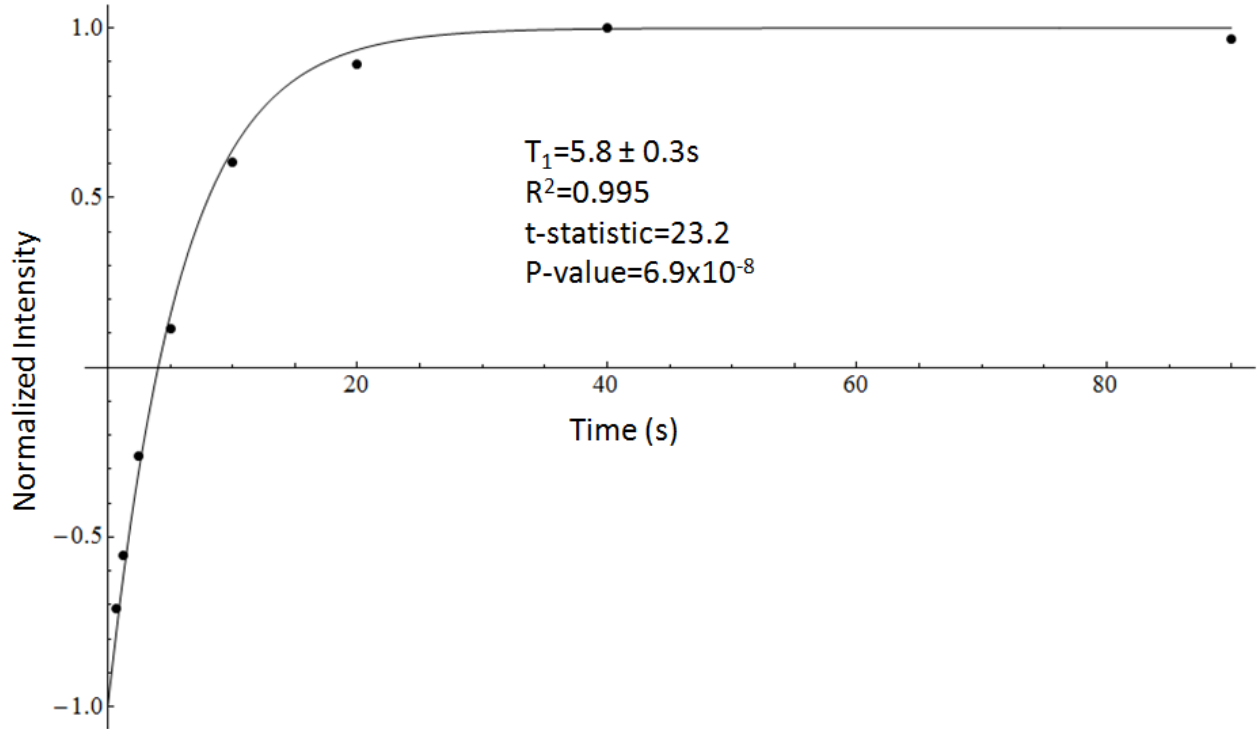


Figure 6-5. Inversion recovery experiments on Xe gas reference sample at 25°C

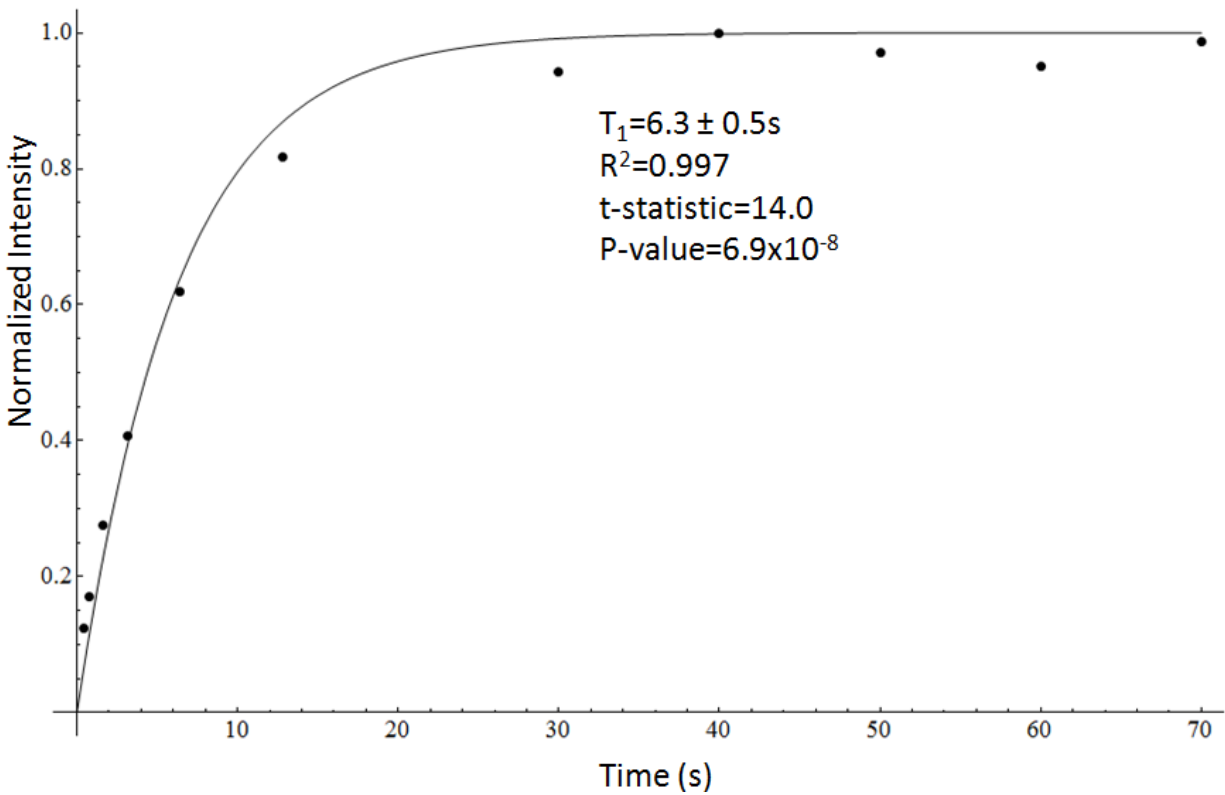


Figure 6-6. Saturation recovery experiments on Xe gas reference sample at 25°C

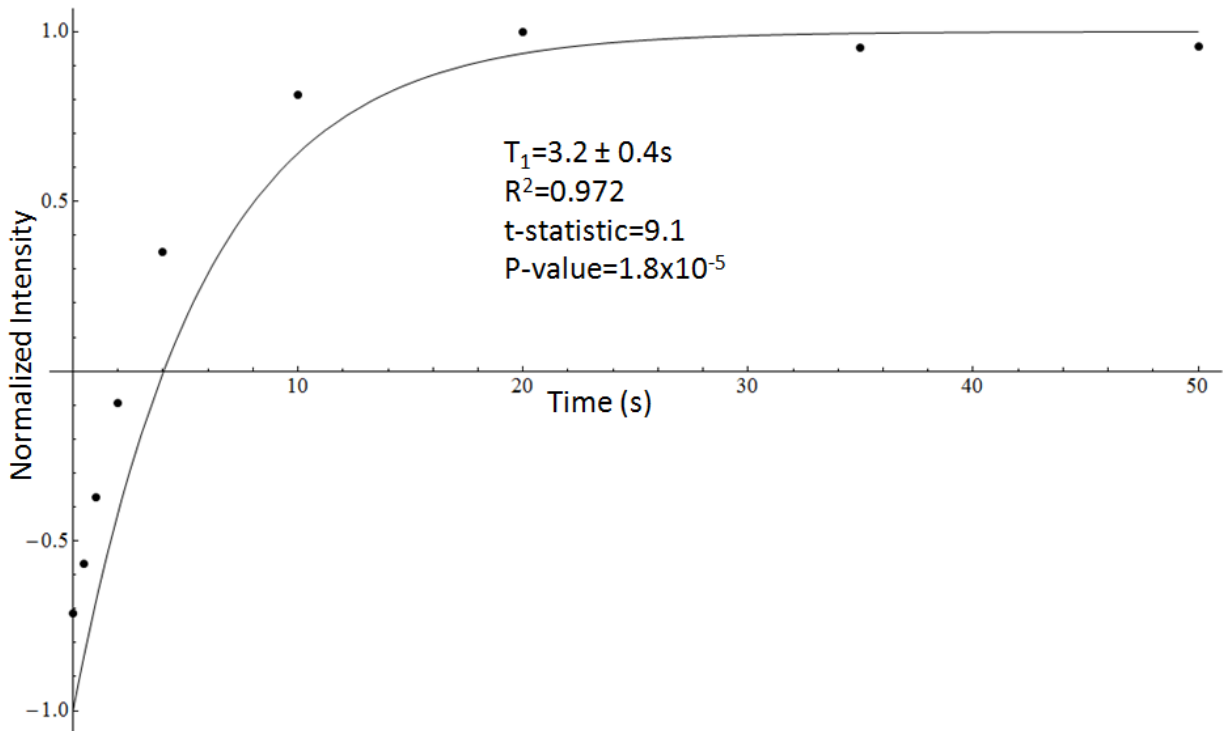


Figure 6-7. Inversion recovery experiments on Xe gas reference sample at -85°C

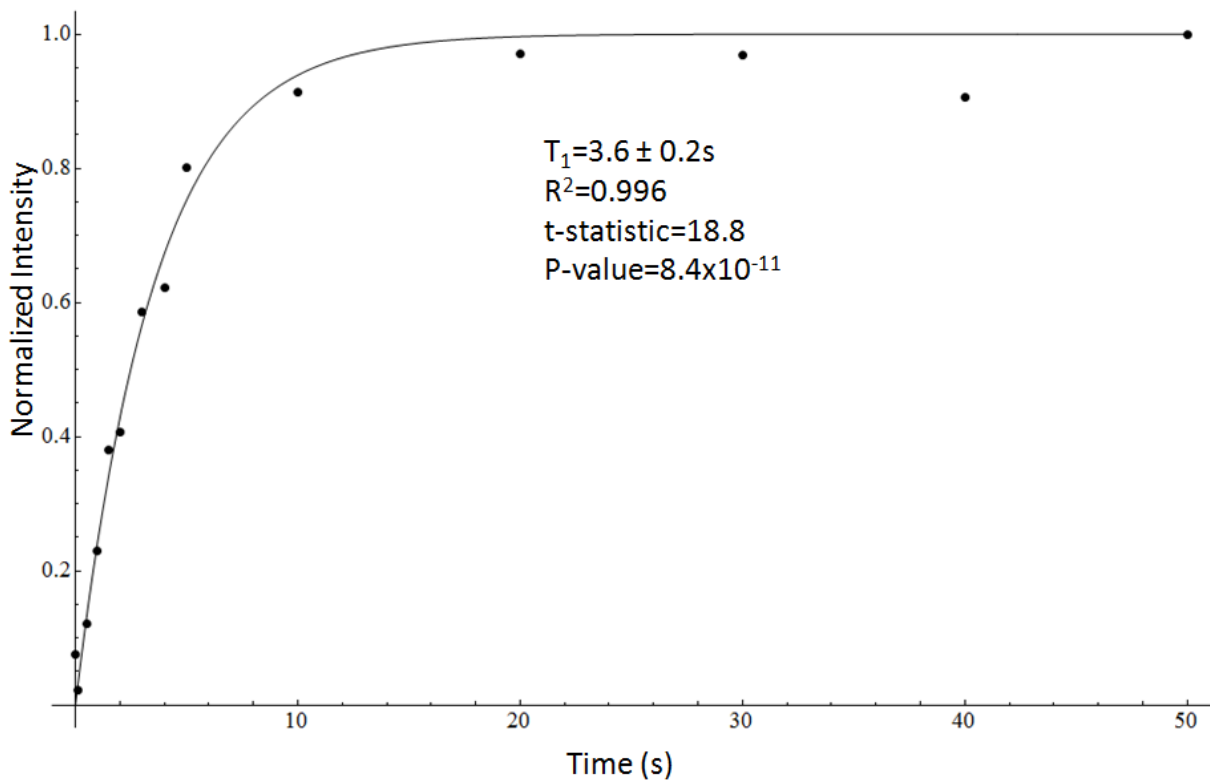


Figure 6-8. Saturation recovery experiments on Xe gas reference sample at -85°C

As noticed in Figures 6-5 – 6-8, T_1 decreases with decreasing temperature. In 1988, a report was published studying the nuclear spin relaxation by intermolecular magnetic dipole coupling in the gas phase for mixtures of ^{129}Xe in oxygen.⁴² This study came to the conclusion that T_1 relaxation rates are dependent on temperature, however, it was concluded that the specific temperature dependence could not be very precisely determined by the experiments. The temperature dependence from this study is shown in Figure 6-9. As can be seen, as the temperature is decreased for a constant density of oxygen, $1/T_1$ increases meaning that T_1 decreases, which is a similar trend seen in the above experimental results at 25 and -85°C .

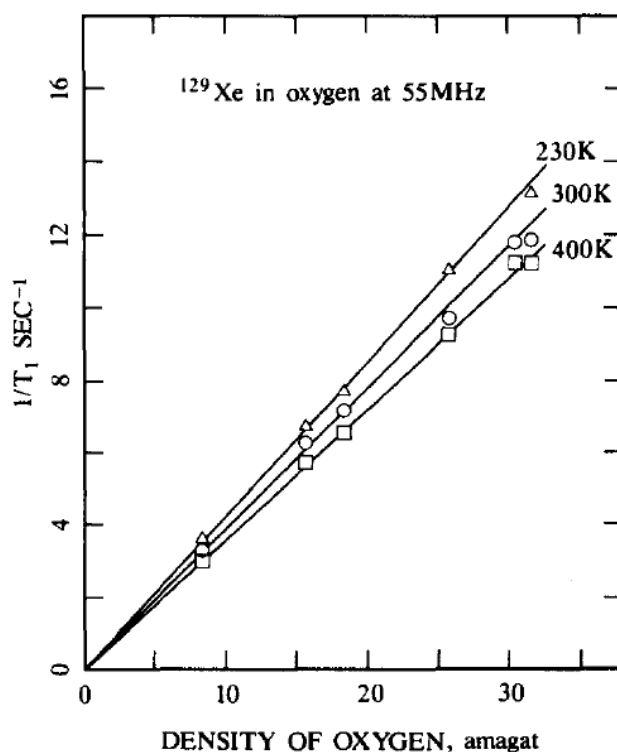


Figure 6-9. Density and temperature dependence of ^{129}Xe spin relaxation times. [Image reproduced with permission from Jameson, J.C.; Jameson, A.K.; Hwang, J.K. *Journal of Chemical Physics* 1988, 89 (Page 4075, Figure 3). American Institute of Physics.]

In another study conducted in 1995, the longitudinal relaxation time of the ^{129}Xe nucleus of natural xenon gas dissolved in various liquids was studied as a function of temperature.⁴³ This study came to the conclusion that the T_1 relaxation increases with increasing temperature, which corresponds to the same trend that is seen in the xenon reference sample of Figures 6-5 – 6-8. This publication proposed that the relaxation mechanisms of the ^{129}Xe nucleus in gases and solutions are exclusively due to intermolecular interactions. In the gas phase, relaxation comes from the spin-rotation coupling during atomic collisions or during the transient existence of diatomic molecules. Other possible relaxation mechanisms in xenon include diffusion through magnetic field gradients caused by a host, wall interactions, and relaxation with other xenon atoms.

The saturation recovery experiments performed on FF at -85°C and -95°C for the small and large channels are shown in Figures 6-10 – 6-13.

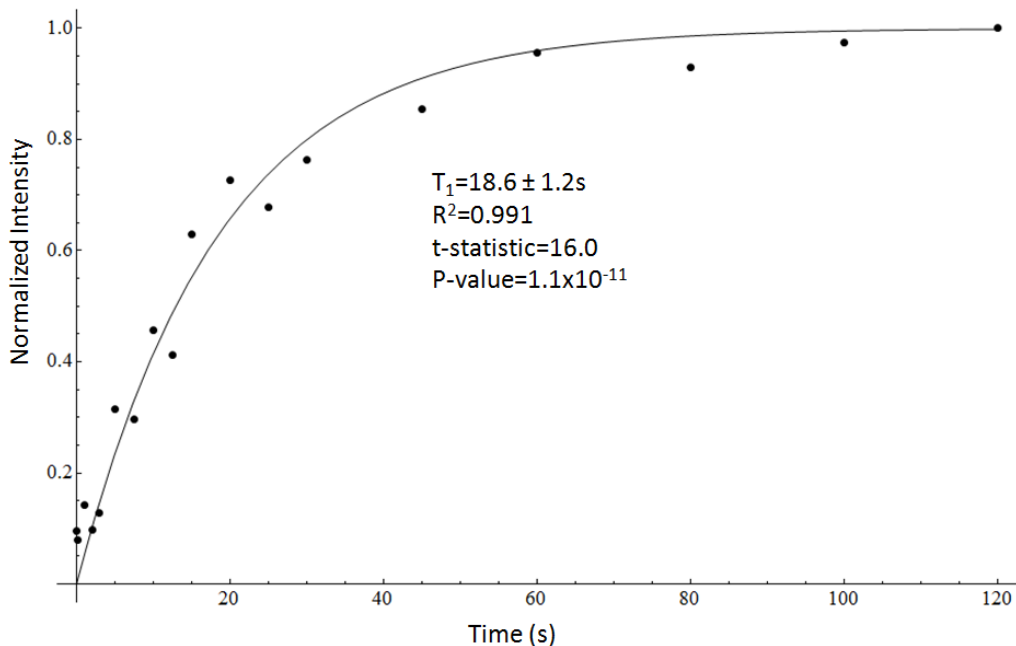


Figure 6-10. Saturation recovery experiments on the small channels of FF nanotubes at -85°C

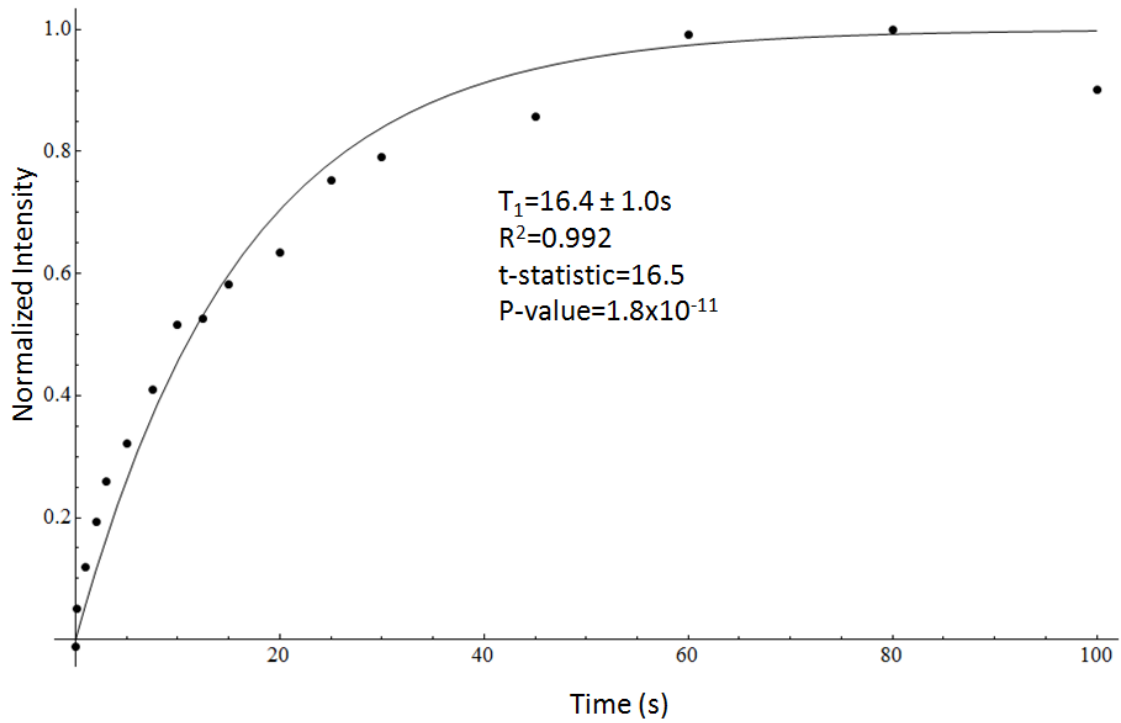


Figure 6-11. Saturation recovery experiments on the small channels of FF nanotubes at -95°C

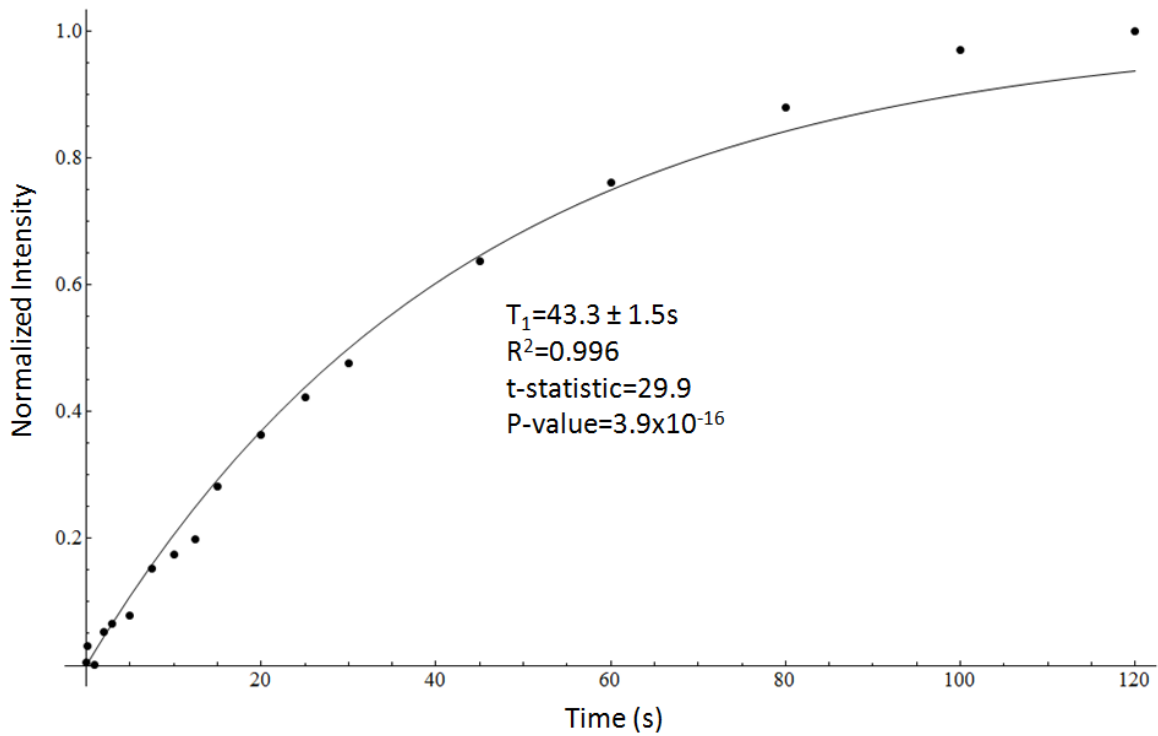


Figure 6-12. Saturation recovery experiments on the large channels of FF nanotubes at -85°C

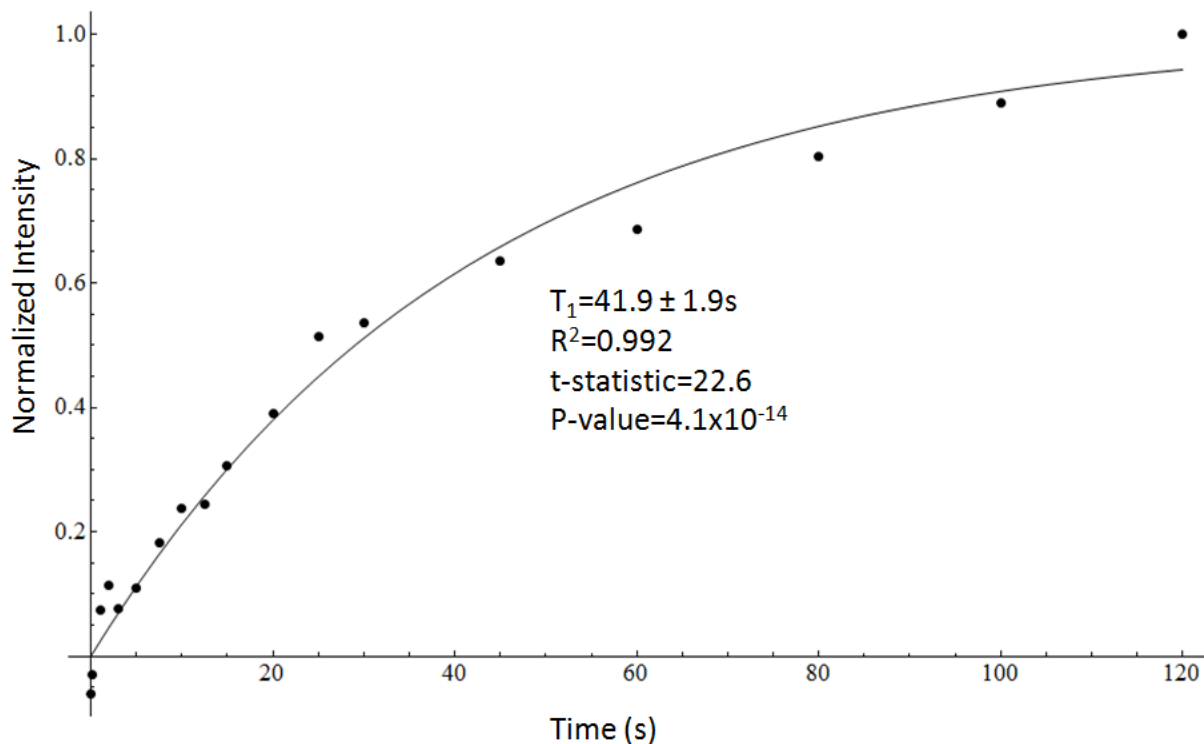


Figure 6-13. Saturation recovery experiments on the large channels of FF nanotubes at -95°C

Table 6-1. Summary table of T_1 relaxation times

Sample	Method	Temperature (°C)	Channel	T_1 (seconds)
FF	Sat. Rec.	-85	Small	18.6±1.2
			Large	43.3±1.5
	Tracer-Exchange	-95	Small	16.4±1.0
			Large	41.9±1.9
	Tracer-Exchange	-93 (questionable)	Small	5.4±0.3
			Large	3.6±0.4
Xe Reference	Sat. Rec.	25		6.3±0.5
		-85		3.6±0.2
	Inv. Rec.	25		5.8±0.3
		-85		3.2±0.4

As was the case with the xenon gas reference sample, the channels in the FF nanotubes also show a T_1 temperature dependence where the relaxation time decreases with decreasing temperature. It should be noted, however, that relaxation

mechanisms in the bulk and adsorbed phases may be different. The decrease in T_1 observed here is substantially less when compared to the reference sample considering it is only over a 10°C range as opposed to the 110°C range that was used for the reference.

One noticeable difference here is the trend in the T_1 values between the FF saturation recovery experiments and the FF tracer-experiments. In the saturation recovery experiments, for the same temperature, the T_1 of the large channel is greater than that of the small channel. However, in the tracer-exchange experiments, the T_1 of the large channel is smaller than that of the small channel. This investigation is ongoing and no clear explanation for this discrepancy currently exists.

Bis-Urea Macrocycle

Xenon partial-pressure dependence

The first experiments performed on the bis-urea macrocycle constituted a xenon partial-pressure dependence study, which is shown in Figure 6-14. At low-pressure/loading, the chemical shift powder pattern shows a very large anisotropy and is opposite in sign to that observed in other single-file materials at low-loading.^{44,45} At higher pressures, the shielding anisotropy decreases and appears to reverse sign near the highest pressure studied due to Xe-Xe interactions.

The chemical shift anisotropy of the xenon atom should be observed as an average over the volume sampled due to rapid movement of the xenon atom. However, if xenon were static at some site on the pore wall, a large anisotropy may be observed. In 1995, the anisotropic chemical shift of ^{129}Xe in the aluminophosphate molecular sieve ALPO-11, shown in Figure 6-15, was studied.⁴⁶ The dependence of the chemical shift trapped in the one dimensional pores was measured as a function of xenon loading.

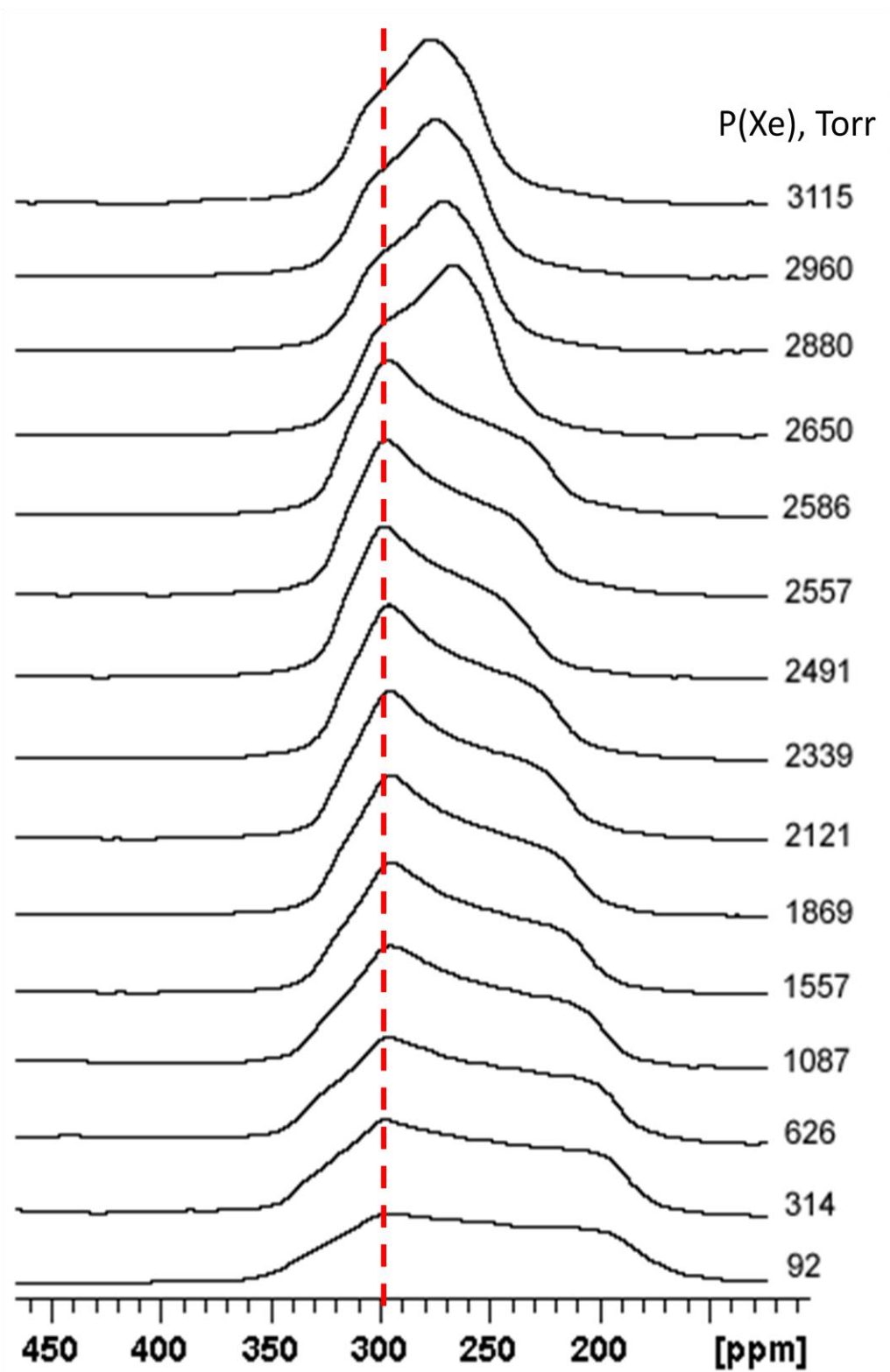


Figure 6-14. Dependence of the ^{129}Xe line shape in the one-dimensional pores of bis-urea crystals on Xe partial pressure in a He/Xe mixture with a total pressure of 3115 Torr

The anisotropy was found to be axially symmetric and positive at low loading and then it appeared to lose its axial symmetry with increased loading. However, at even higher loading, an axial line shape again was observed but the sign was reversed from the previous time with nonaxial line shapes at intermediate and high loadings. Two principal components of the observed shielding tensor were found to vary linearly with Xe loading while a third remained invariant. This behavior of the line shape was analyzed in terms of a statistical distribution of three types of xenon sites. Each of these sites had 0, 1, or 2 neighboring sites occupied by other Xe atoms, shown in Figure 6-16. Each site also possessed its own characteristic shielding tensor, and fast exchange of the three site types at room temperature was assumed.⁴⁵ The experimental results of this study are shown in Figure 6-17 and provide a decent comparison to the results obtained in the bis-urea macrocycle.

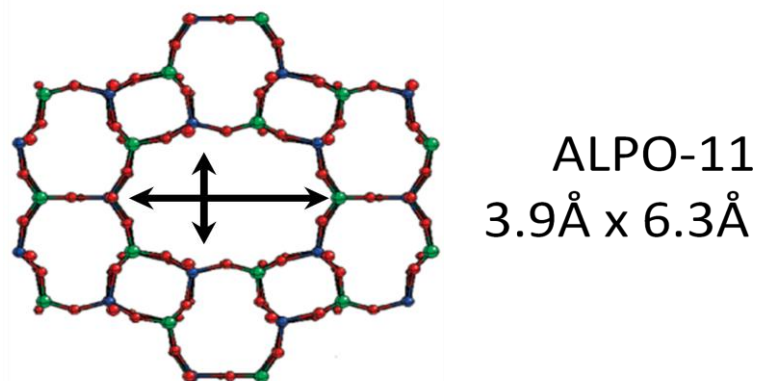


Figure 6-15. Structure and channel diameter of ALPO-11.

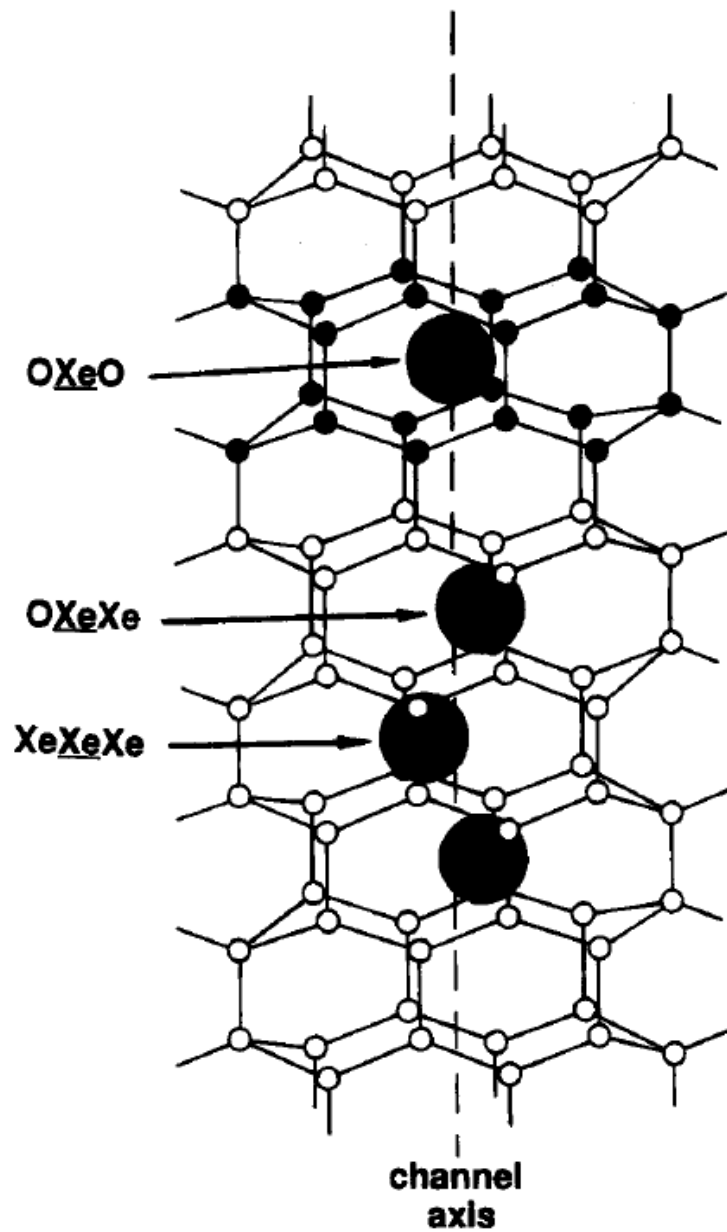


Figure 6-16. Structure of one channel in ALPO-11 indicating the three types of xenon sites. [Image reproduced with permission from Ripmeester, J.A.; Ratcliffe, C.I. *Journal of Physical Chemistry* 1995, 99 (Page 621, Figure 3). American Chemical Society.]

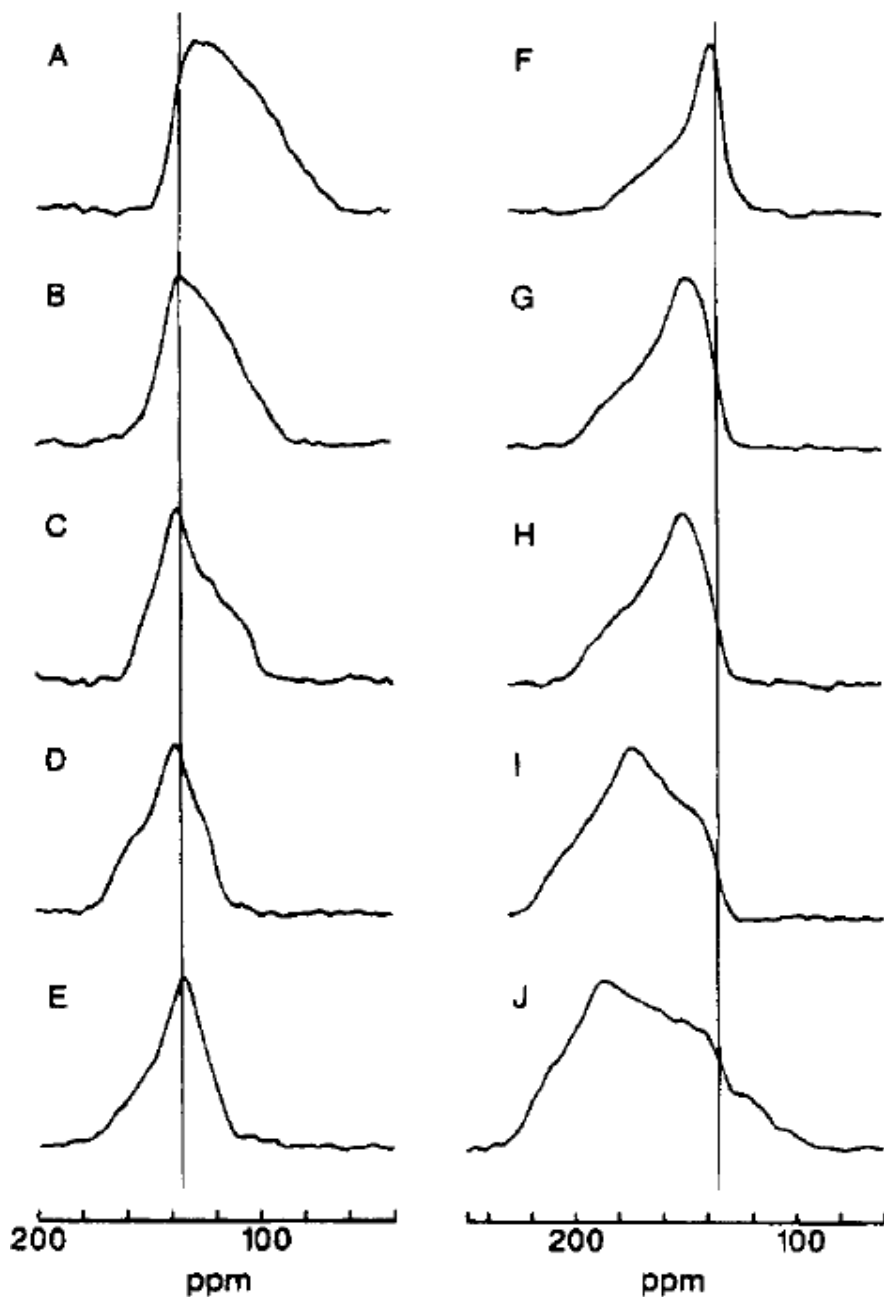


Figure 6-17. ^{129}Xe NMR line shapes for xenon adsorbed in ALPO-11. Loading levels: A=1.58, B=2.70, C=3.80, D=5.16, E=5.83, F=8.05, G=10.30, H=11.10, I=13.40, J=16.40 mol of Xe ($\times 10^{-4}$)/g of dry ALPO-11. [Image reproduced with permission from Ripmeester, J.A.; Ratcliffe, C.I. *Journal of Physical Chemistry* 1995, 99 (Page 620, Figure 1). American Chemical Society.]

In 1989, a magic angle spinning NMR study on the silicoaluminophosphate molecular sieve SAPO-11, which is structurally similar to ALPO-11, concluded that the

xenon static line shapes arose from a single anisotropic chemical shift interaction.⁴⁵

The variations in this anisotropy were attributed to changes/deformations in the shape of the electron cloud around the xenon atom as more and more atoms were packed into the elliptical nanochannel. This could potentially be the case with the bis-urea macrocycle, as deformations in the electron cloud seem even more likely given the smaller elliptically-shaped nanochannels.

Another possible explanation for these lineshapes is that the three components of the chemical shift shielding tensor may be different. In the case of a cylindrically symmetric nanochannel, two components of the tensor are identical with the third being different. However, being that the bis-urea channels are elliptical and not cylindrically symmetric, it is possible and plausible that each of these three components is different, and an averaging of these three tensors could account for the observed lineshapes.

Tracer-Exchange

Tracer-exchange experiments were performed on the bis-urea sample to probe xenon dynamics upon the adsorption process. The data for this, collected at room temperature, is shown in Figure 6-18. This data was fit to the tracer exchange functions mentioned in Chapter 5, and the fits to normal and single-file diffusion are shown in Figure 6-19.

As seen in Figure 6-19, the bis-urea data visually seems to fit the tracer-exchange function (Eq. [5-4]) for single-file diffusion better than for normal diffusion. However, the statistics and error between the two fits are too close to determine which one is actually better. Single-file diffusion is expected given the channel diameter of the sample as $3.7 \times 4.8 \text{ \AA}$ and the collision diameter of xenon as 4.4 \AA . Within this narrow channel, two

xenon atoms would not be predicted to pass one another based on simple geometry. T_1 measurements through thermally-polarized xenon saturation recovery experiments at room temperature could help distinguish which fit is more accurate but the amount of sample available was insufficient for these experiments. This remains an ongoing investigation.

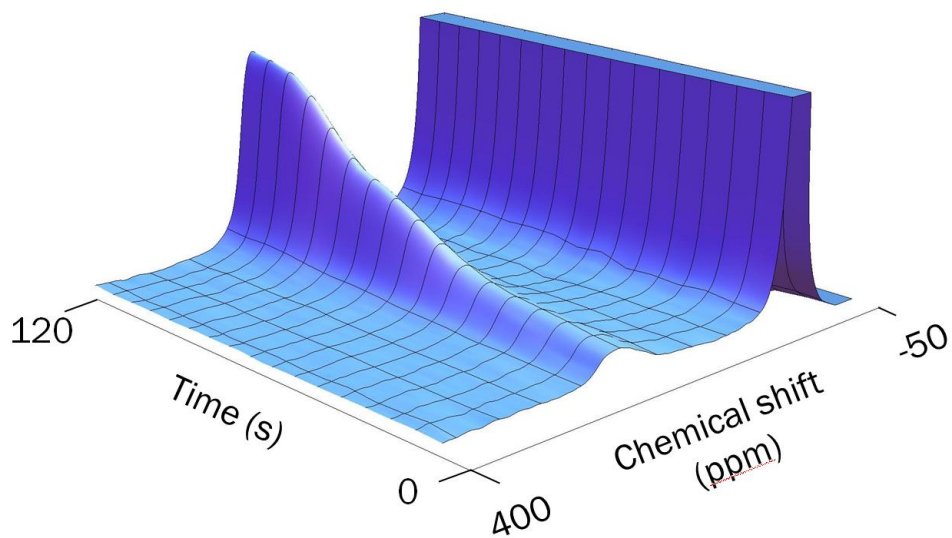


Figure 6-18. Tracer-exchange data on bis-urea macrocycle

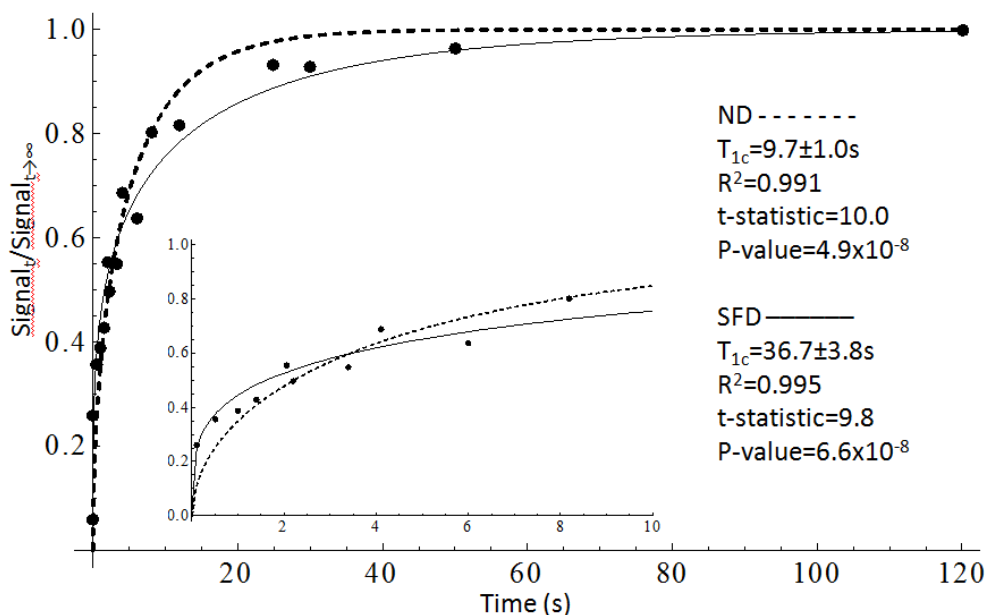


Figure 6-19. Tracer-exchange fits for the bis-urea macrocycle

CHAPTER 7 CONCLUSION AND RECOMMENDATIONS

The FF tracer exchange studies conducted clearly demonstrated the observance of normal diffusion within the two different sized nanochannels. An attempt was made to verify the T_1 relaxation times extracted from these fits utilizing thermally-polarized xenon saturation and inversion recovery experiments at a similar temperature and pressure. It was found that at -75°C , no xenon adsorption into the smaller channel of FF was observed using thermally-polarized xenon which opposed the results of the hyperpolarized tracer-exchange experiments. However, adsorption into the smaller channel was observed at -85°C . A possible reason for this temperature discrepancy is the heating of the sample cause by the gas stream during the continuous-flow hyperpolarized ^{129}Xe experiments. This can be rectified through a temperature calibration.⁴⁷

In studying the xenon adsorption at various temperatures, it was found that the chemical shift decreases with increasing temperature which is in agreement with similar results found throughout the literature. It was also determined that at decreasing temperatures, xenon migrates from the large, central channel to the small, narrow channel of the FF nanotubes. One possible explanation for this is that at reduced temperatures, condensation occurs in the smaller channels and a liquid phase is observed, as this would be thermodynamically-favored to occur in the smaller channels as opposed to the larger channels.

For the xenon gas reference sample and the FF nanotubes, the T_1 relaxation decreased with decreasing temperature, albeit the two systems may have different

relaxation mechanisms. This was also in line with results found throughout the literature.

The bis-urea macrocycle pressure study demonstrated that the anisotropy was axially symmetric and positive at low loading and then lost its axial symmetry with increased loading. *Ab-initio* calculations of ^{129}Xe shielding tensors could possibly account for the chemical shift powder patterns and the Xe loading dependence.

The tracer-exchange experiments for the bis-urea were not conclusive as to which type of diffusion is occurring in the channel. However, single-file diffusion is expected given the channel geometry. A larger bis-urea macrocycle possessing a channel diameter around 10\AA has recently been synthesized and is awaiting experimentation. It is expected that this sample will exhibit normal diffusion given its channel size. With this sample, verification of T_1 values through thermally-polarized xenon experiments would prove beneficial.

LIST OF REFERENCES

- (1) Karger, J.; Ruthven, D.M. *Diffusion in Zeolites and Other Microporous Solids*; Wiley, 1992.
- (2) Goodson, B.M. *Journal of Magnetic Resonance* **2002**, 155, 157.
- (3) Springuel-Huet, M.A.; Fraissard, J.P. *Zeolites* **1992**, 12, 841.
- (4) Raftery, D.; Long, H.; Meersmann, T.; Grandinetti, P.J.; Reven, L.; Pines, A. *Physical Review Letters* **1991**, 66, 584.
- (5) Jameson, C.J.; de Dios, A.C. *Journal of Chemical Physics* **2002**, 116, 3805.
- (6) Brunner, E. *Protein Science* **2005**, 14, 847.
- (7) Oros, A.M.; Shah, J. *Physics in Medicine and Biology* **2004**, 49, R105.
- (8) Zook, A.L.; Adhyaru, B.B.; Bowers, C.R. *Journal of Magnetic Resonance* **2002**, 159, 175.
- (9) Levitt, M.H. *Spin Dynamics: Basics of Nuclear Magnetic Resonance*; John Wiley & Sons, 2008.
- (10) Ito, T.; Fraissard, J. *Journal of Chemical Physics* **1982**, 76, 5225.
- (11) Cheng, C.Y. PhD Dissertation, University of Florida, **2008**.
- (12) Appelt, S.; Baranga, B.A.; Erickson, C.J.; Romalis, M.V.; Young, A.R.; Happer, W. *Physical Review A* **1998**, 58, 1412.
- (13) Kastler, A. *Journal of the Optical Society of America* **1957**, 47, 460.
- (14) Whiting, N.; Eschmann, N.A.; Goodson, B.M. *Physical Review A* **2011**, 83, 053428.
- (15) Walker, T.G.; Happer, W. *Reviews of Modern Physics* **1997**, 69, 629.
- (16) Raftery, D.; Long, H.; Meersmann, T.; Grandinetti, P.J.; Reven, L.; Pines, A. *Physical Review Letters* **1991**, 66, 584.
- (17) Zook, A.L.; Adhyaru, B.B.; Bowers, C.R. *Journal of Magnetic Resonance* **2002**, 159, 175.
- (18) Rosen, M.S.; Chupp, T.E.; Coulter, K.P.; Welsh, R.C.; Swanson, S.D. *Review of Scientific Instruments* **1999**, 70, 1546.

- 19) Ruest, I.C.; Ketel, S.; Hersman, F.W. *Physical Review Letters* **2006**, *96*, 053002.
- 20) Gorbitz, C.H. *Chemical Communications* **2006**, 2332.
- 21) Reches, M.; Gazit, E. *Science* **2003**, *300*, 625.
- 22) Kol, N.; Adler-Abramovich, L.; Barlam, D.; Shneck, R.Z.; Gazit, E.; Rousso, I. *Nano Letters* **2005**, *5*, 1346.
- 23) Song, Y.; Challa, S.R.; Medforth, C.J.; Qiu, Y.; Watt, R.K.; Pena, D.; Miller, J.E.; Swol, F.; Shelnett, J.A. *Chemical Communications* **2004**, 1044.
- 24) Adler-Abramovich, L.; Reches, M.; Sedman, V.L.; Allen, S.; Tendler, S.J.; Gazit, E. *Langmuir* **2006**, *22*, 1313.
- 25) Reches, M.; Gazit, E. *Nano Letters* **2004**, *4*, 581.
- 26) Makin, O.S.; Atkins, E.; Sikorski, P.; Johansson, J.; Serpell, L.C. *Proceedings of the National Academy of Sciences* **2005**, *102*, 315.
- 27) Gorbitz, C.H. *European Journal of Chemistry* **2001**, *7*, 5153.
- 28) Adler-Abramovich, L.; Aronov, D.; Beker, P.; Yevnin, M.; Stemper, S.; Buzhansky, L.; Rosenman, G.; Gazit, E. *Nature Nanotechnology* **2009**, *4*, 849.
- 29) Ryu, J.; Park, C.B. *Chemistry of Materials* **2008**, *20*, 4284.
- 30) Reches, M.; Gazit, E. *Nature Nanotechnology* **2006**, *1*, 195.
- 31) Shimizu, L.S.; Smith, M.D.; Hughes, A.D.; Shimizu, K.D. *Chemical Communications* **2001**, 1592.
- 32) Dewal, M.B.; Lufaso, M.W.; Hughes, A.D.; Samuel, S.A.; Pellechia, P.; Shimizu, L.S. *Chemistry of Materials* **2006**, *18*, 4855.
- 33) Hahn, E.L. *Physical Review* **1950**, *80*, 580.
- 34) Carr, H.Y.; Purcell, E.M. *Physical Review* **1954**, *94*, 630.
- 35) Aguilar, J.A.; Nilsson, M.; Bodenhausen, G.; Morris, G.A. *Chemical Communications* **2012**, *48*, 811.
- 36) Meersmann, T.; Logan, J.W.; Simonutti, R.; Caldarelli, S.; Comotti, A.; Sozzani, P.; Kaiser, L.G.; Pines, A. *Journal of Physical Chemistry A* **2000**, *104*, 11665.

- 37) Bowers, C.; Cheng, C. *Chem. Phys. Chem.* **2007**, *8*, 2077.
- 38) Vasenkov, S.; Karger, J. *Physical Review E* **2002**, *66*, 052601.
- 39) Jeener, J.; Meier, B.H.; Bachmann, P.; Ernst, R.R. *Journal of Chemical Physics* **1979**, *71*, 4546.
- 40) Blumich, B. *NMR Imaging of Materials*; Oxford University Press, 2000.
- 41) Cheung, T.T.P. *Journal of Physical Chemistry* **1995**, *99*, 7089.
- 42) Jameson, J.C.; Jameson, A.K.; Hwang, J.K. *Journal of Chemical Physics* **1988**, *89*, 4074.
- 43) Oikarinen, K.; Jokisaari, J. *Applied Magnetic Resonance* **1995**, *8*, 587.
- 44) Jameson, C.J.; de Dios, A.C. *Journal of Chemical Physics* **2002**, *116*, 3805.
- 45) Springuel-Huet, M.A.; Fraissard, J. *Journal of Chemical Physics Letters* **1989**, *154*, 299.
- 46) Ripmeester, J.A.; Ratcliffe, C.I. *Journal of Physical Chemistry* **1995**, *99*, 619.
- 47) Kneller, J.M.; Soto, R.J.; Surber, S.E.; Colomer, J.F.; Fonseca, A.; Nagy, J.B.; Pietraß, T. *Journal of Magnetic Resonance* **2000**, *147*, 261.

BIOGRAPHICAL SKETCH

Christopher Akel was born in Jacksonville, Florida in 1987. He received his B.S. degree in chemistry with a minor in physics from Barry University located in Miami Shores, Florida, in 2009. He joined Dr. Russ Bowers' research group at the University of Florida during the summer of 2009 to pursue his M.S. degree in physical chemistry. Since then, he has worked full-time as a graduate student and teaching assistant. Since entering graduate school, he has been involved in several projects including solid-state deuterium NMR studies of polymers, ^{23}Na magic-angle spinning NMR of polycrystalline $\text{Na}_{24}\text{Si}_{136}$, rubidium optical pumping at high magnetic fields, hyperpolarized ^{129}Xe NMR in nanotubular materials, and numerous crystallization projects. His current research interests include solid-state NMR and hyperpolarized noble gas NMR. After graduation in 2012, he plans to enter the work-force in the chemical industry business.